

Lattice QCD approach to Nuclear Physics

Sinya AOKI^{1,2}, Takumi DOI³, Tetsuo HATSUDA^{3,4}, Yoichi IKEDA⁵, Takashi INOUE⁶,
Noriyoshi ISHII², Keiko MURANO³, Hidekatsu NEMURA², Kenji SASAKI² (HAL
QCD Collaboration)

¹*Graduate School of Pure and Applied Sciences, University of Tsukuba,
Tsukuba 305-8571, Japan*

²*Center for Computational Sciences, University of Tsukuba,
Tsukuba, 305-8577, Japan*

³*Theoretical Research Division, Nishina Center, RIKEN, Wako 351-0198, Japan*

⁴*IPMU, The University of Tokyo, Kashiwa 277-8583, Japan*

⁵*Department of Physics, Tokyo Institute of Technology, Tokyo 152-8551, Japan*

⁶*Nihon University, College of Bioresource Sciences, Fujisawa 252-0880, Japan*

We review recent progress of the HAL QCD method which was recently proposed to investigate hadron interactions in lattice QCD. The strategy to extract the energy-independent non-local potential in lattice QCD is explained in detail. The method is applied to study nucleon-nucleon, nucleon-hyperon, hyperon-hyperon and meson-baryon interactions. Several extensions of the method are also discussed.

§1. Introduction

One of the ultimate goals in nuclear physics is to describe hadronic many-body problems on the basis of the hadronic S-matrices calculated from first principle QCD. In particular, the nuclear forces are the most fundamental quantities: Once they are obtained from QCD, one can solve finite nuclei, hypernuclei, nuclear matter and hyperon matter by employing various many-body techniques developed in nuclear physics.

Phenomenological nucleon-nucleon (NN) potentials, which are designed to reproduce a large number of proton-proton and neutron-proton scattering data as well as deuteron properties have been constructed in 90's and are called high-precision NN potentials. Some of the examples are shown in Fig. 1, which reflect characteristic features of the NN interaction for different values of the relative distance r as reviewed in 1)–5):

The long range part of the NN force ($r > 2$ fm) is dominated by one-pion exchange originally introduced by Yukawa.¹⁰⁾ Since the pion is the Nambu-Goldstone boson associated with the spontaneous breaking of chiral symmetry, it couples to the nucleon's spin-isospin density and leads to not only the central force but also the tensor force. The medium range part ($1 \text{ fm} < r < 2 \text{ fm}$) of the NN force receives significant contributions from two-pion ($\pi\pi$) exchange¹¹⁾ and/or heavy meson (ρ , ω , and σ) exchanges. In particular, the spin-isospin independent attraction of about 50 – 100 MeV in this region plays an essential role to bind the atomic nuclei and nuclear matter. The short range part ($r < 1$ fm) of the NN force is best described by a phenomenological repulsive core introduced by Jastrow.¹²⁾

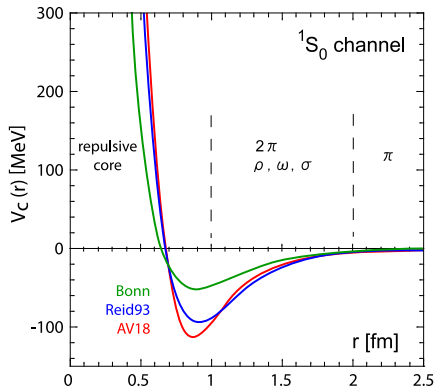


Fig. 1. Three examples of the modern NN potential in 1S_0 (spin-singlet and S -wave) channel: Bonn,⁶⁾ Reid93⁷⁾ and Argonne v_{18} .⁸⁾ Taken from Ref. 9).

The nuclear saturation, the nuclear shell structure, the nuclear superfluidity and the structure of neutron stars are all related to the properties of the nuclear force.^{13)–15)} Furthermore, the hyperon-nucleon (YN) and hyperon-hyperon (YY) forces, whose information is still quite limited experimentally, are crucial to understand the structure of hypernuclei and the core of the neutron stars. The three-nucleon forces (and the three-baryon forces in general) are also important to understand the binding energies of finite nuclei and the equation of state of dense hadronic matter.

It has been a long-standing challenge in theoretical particle and nuclear physics to extract the hadron-hadron interactions from first principle. A framework suitable for such a purpose in lattice QCD was first proposed by Lüscher:¹⁶⁾ For two hadrons in a finite box with the size $L \times L \times L$ under periodic boundary conditions, an exact relation between the energy spectra in the box and the elastic scattering phase shift at these energies has been derived. If the range of the hadron interaction R is sufficiently smaller than the size of the box $R < L/2$, the behavior of the two-particle Nambu-Bethe-Salpeter (NBS) wave function $\varphi(\mathbf{r})$ in the interval $R < |\mathbf{r}| < L/2$ is sufficient to relate the phase shift and the two-particle spectrum. This Lüscher’s finite volume method bypasses the difficulty to treat the real-time scattering process on the Euclidean lattice. Furthermore, it utilizes the finiteness of the lattice box effectively to extract the information of the on-shell scattering matrix and the phase shift.

A closely related but a new approach to the hadron interactions from lattice QCD has been proposed recently by three of the present authors^{9),17),18)} and has been developed extensively by the HAL QCD Collaboration. (Therefore the approach is now called the HAL QCD method.) Its starting point is the same NBS wave function $\varphi(\mathbf{r})$ as discussed in Ref. 16). Instead of looking at the wave function outside the range of the interaction, the authors consider the internal region $|\mathbf{r}| < R$ and define an integral kernel (or the non-local “potential” in short) $U(\mathbf{r}, \mathbf{r}')$ from $\varphi(\mathbf{r})$ so that it obeys the Schrödinger type equation in a finite box. This potential can be shown to be energy-independent by construction. Since $U(\mathbf{r}, \mathbf{r}')$ for strong

interactions is localized in its spatial coordinates due to confinement of quarks and gluons, it receives only weak finite volume effect in a large box. Therefore, once U is determined and is appropriately extrapolated to $L \rightarrow \infty$, one may simply use the Schrödinger type equation in infinite space to calculate the scattering phase shifts and bound state spectra to compare the results with experimental data. Since U is a smooth function of the quark masses, it is relatively easy to handle on the lattice. This is in sharp contrast to the scattering length, which shows a singular behavior in the quark mass corresponding to the formation of the hadronic bound state. A further advantage of the HAL QCD method is that it can be generalized directly to the many-body forces and also to the case of inelastic scattering.

Studying structure of S (strangeness) = -1 and $S = -2$ hypernuclei is one of the key challenges in modern nuclear physics. Also, the central core of the neutron stars will have hyperonic matter if the neutron beta-decays to hyperons become possible at high density. The hyperon-nucleon (YN) and hyperon-hyperon (YY) interactions are crucial to determine the level structures of hypernuclei as well as onset-density of hyperonic matter in neutron stars.¹⁹⁾ By generalizing the NN scattering in the flavor $SU(2)$ space to the baryon-baryon (BB) scatterings in the flavor $SU(3)$ space, the HAL QCD method can give the YN and YY potentials as natural extension of the NN potentials. Such extension is also useful for identifying the origin of the short-range repulsive core of the NN potential and for studying possible $S = -2$ six-quark state such as the H -dibaryon.

In this article, we review the basic ideas and recent progress of the HAL QCD method to hadron interactions. (As for the Lüscher's finite volume method, see a recent review Ref. 20.) In Sec. 2, the basic strategy to define the NN potential in QCD is explained. In Sec. 3, we introduce lattice formulations of the time-independent HAL QCD method originally proposed in Refs.9), 17), 18) as well as its time-dependent generalization. In Sec. 4, some recent results of lattice QCD calculations for the NN potential are given in both quenched and full QCD. Magnitude of the non-locality in U is also discussed in the section. In Sec. 5, the method is applied to the hyperon-nucleon interactions such as $N\Xi$ and $N\Lambda$ systems. In Sec. 6, interactions between octet baryons are investigated in the flavor $SU(3)$ limit, where up, down and strange quark masses are all equal. In Sec. 7, a generalization of the HAL QCD method to the case of inelastic scattering is given. In Sec. 8, we show results of the three-nucleon potential, especially its short distant structure. In Sec. 9, an application to the kaon-nucleon scattering is considered. Sec. 10 is devoted to summary and concluding remarks.

§2. Defining the potential in QCD

2.1. Nambu-Bethe-Salpeter (NBS) wave function

A key quantity to define the baryon-baryon(BB) "potential" in QCD is the equal-time Nambu-Bethe-Salpeter wave function,

$$\varphi^W(\mathbf{x})e^{-Wt} = \langle 0|T\{B(\mathbf{r} + \mathbf{x}, t)B(\mathbf{r}, t)\}|2B, W, s_1 s_2\rangle, \quad (2.1)$$

where $|2B, W, s_1 s_2\rangle$ is a QCD eigenstate for two baryons with equal mass m_B , helicity s_1 and s_2 , total energy $W = 2\sqrt{\mathbf{k}^2 + m_B^2}$, the relative momentum \mathbf{k} , and the total momentum \mathbf{p} (we take $\mathbf{p} = 0$ in this paper). Generalization to the unequal mass can be formulated in a similar manner. In the case of two nucleons, the local interpolating operator $B(x)$ is taken as

$$B_\alpha(x) \equiv \begin{pmatrix} p_\alpha(x) \\ n_\alpha(x) \end{pmatrix} = \varepsilon_{abc} (u_a^T(x) C \gamma_5 d_b(x)) q_{c,\alpha}(x), \quad q(x) = \begin{pmatrix} u(x) \\ d(x) \end{pmatrix}, \quad (2.2)$$

where $x = (\mathbf{x}, t)$, a, b, c are the color indices, and α is the spinor index. The charge conjugation matrix is given by $C = \gamma_2 \gamma_4$, and p, n are proton and neutron operators while u, d denote up and down quark operators. Here φ^W implicitly has two pairs of spinor-flavor indices from $B_\alpha(\mathbf{r} + \mathbf{x}, t) B_\beta(\mathbf{r}, t)$ as well as two helicity indices s_1 and s_2 .

The most important property of the above NBS wave function is as follows. If the total energy W lies below the threshold of meson production (*i.e.* $W < 2m_B + m_M$ with the meson mass m_M), it satisfies the Helmholtz equation with $k = |\mathbf{k}|$ at $r = |\mathbf{r}| \rightarrow \infty$,

$$[k^2 + \nabla^2] \varphi^W(\mathbf{r}) \simeq 0. \quad (2.3)$$

Furthermore, the asymptotic behavior of the radial part of the NBS wave function for given orbital angular momentum L and total spin S reads^{18),21)}

$$\varphi^W(r; LS) \propto \frac{\sin(kr - L\pi/2 + \delta_{LS}(k))}{kr} e^{i\delta_{LS}(k)}. \quad (2.4)$$

Here $\delta_{LS}(k)$ is nothing but the phase shift obtained from the baryon-baryon S-matrix in QCD below the inelastic threshold. It should be remarked here that only the upper components of the spinor indices for the NBS wave function ($\alpha = 1, 2$ and $\beta = 1, 2$) are enough to reproduce all BB scattering phase shifts $\delta_{LS}(k)$ with $L = 0, 1, 2, 3, \dots$ and $S = 0, 1$ (See Appendix A of Ref.18) for the precise expression of Eq.(2.4) and its relation to the S-matrix in QCD.)

2.2. Non-local potential from the NBS wave function

From the NBS wave function, we define a non-local potential through the relation^{9),17),18)}

$$(E_k - H_0) \varphi_{\alpha\beta}^W(\mathbf{x}) = \int U_{\alpha\beta;\gamma\delta}(\mathbf{x}, \mathbf{y}) \varphi_{\gamma\delta}^W(\mathbf{y}) d^3y, \quad \left(E_k = \frac{k^2}{2\mu}, H_0 = \frac{-\nabla^2}{2\mu} \right), \quad (2.5)$$

where $U(\mathbf{x}, \mathbf{y})$ is expected to be short-ranged because of absence of massless particle exchanges between two baryons. As mentioned in the previous subsection, it is enough to consider the upper spinor indices of $\alpha, \beta, \gamma, \delta$: Then 16 components of $U_{\alpha\beta;\gamma\delta}$ can be determined from 4 components of $\varphi_{\alpha\beta}^W$ for 4 different combinations of (s_1, s_2) . Since the NBS wave function φ^W is multiplicatively renormalized, the potential $U(\mathbf{x}, \mathbf{y})$ is finite and does not depend on the particular renormalization scheme. Note that, while Lorentz covariance is lost by using the equal-time NBS

wave function and Eq. (2.5) is written as a Schrödinger type equation, no non-relativistic approximation is employed here to define $U(\mathbf{x}, \mathbf{y})$.

The non-local potential $U(\mathbf{x}, \mathbf{y})$ has been shown to be energy-independent.^{17),18)} To see this, let \mathcal{V}_{th} be the space spanned by the wave function at $W \leq W_{\text{th}} \equiv 2m_B + m_M$: $\mathcal{V}_{\text{th}} = \{\varphi_c^W | W \leq W_{\text{th}}\}$ where c represents quantum numbers of the NBS wave function other than energy W . Then the projection operator to \mathcal{V}_{th} is given by

$$\begin{aligned} P^{W_{\text{th}}}(\mathbf{x}, \mathbf{y}) &= \sum_{W_1, W_2 \leq W_{\text{th}}} \sum_{c_1, c_2} \varphi_{c_1}^{W_1}(\mathbf{x}) N_{c_1, c_2}^{-1}(W_1, W_2) \varphi_{c_2}^{W_2}(\mathbf{y})^\dagger \\ &\equiv \sum_{W \leq W_{\text{th}}} \sum_c P_c^{W_{\text{th}}}(W; \mathbf{x}, \mathbf{y}) \end{aligned} \quad (2.6)$$

where $N_{c_1, c_2}^{-1}(W_1, W_2)$ is defined as the inverse of the Hermitian operator

$$N_{c_1, c_2}(W_1, W_2) = \int \varphi_{c_1}^{W_1}(\mathbf{r})^\dagger \varphi_{c_2}^{W_2}(\mathbf{r}) d^3r, \quad W_{1,2} \leq W_{\text{th}}, \quad (2.7)$$

which satisfies

$$\sum_{W \leq W_{\text{th}}} \sum_c N_{c_1, c}(W_1, W) N_{c, c_2}^{-1}(W, W_2) = \delta_{c_1, c_2} \delta_{W_1, W_2} \quad (2.8)$$

in the restricted indices that $W_{1,2} \leq W_{\text{th}}$. (We here assume that $N(W_1, W_2)$ does not have zero eigenvalues in this restricted space.)

Using these, the non-local potential is defined by

$$\begin{aligned} U^{W_{\text{th}}}(\mathbf{x}, \mathbf{y}) &= \sum_{W_{1,2} \leq W_{\text{th}}} \sum_{c_1, c_2} \rho(W_1) [E_k - H_0] \varphi_{c_1}^{W_1}(\mathbf{x}) N_{c_1, c_2}^{-1}(W_1, W_2) \varphi_{c_2}^{W_2}(\mathbf{y})^\dagger \\ &= \sum_{W \leq W_{\text{th}}} \sum_c [E_k - H_0] P_c^{W_{\text{th}}}(W; \mathbf{x}, \mathbf{y}). \end{aligned} \quad (2.9)$$

Then, it is easy to observe that the above non-local potential satisfies Eq.(2.5) at $W \leq W_{\text{th}}$:

$$\begin{aligned} \int U^{W_{\text{th}}}(\mathbf{x}, \mathbf{y}) \varphi_c^W(\mathbf{y}) d^3y &= \sum_{W_1 \leq W_{\text{th}}} \sum_{c_1} [E_k - H_0] \varphi_{c_1}^{W_1}(\mathbf{x}) \delta_{c, c_1} \delta_{W_1, W} \\ &= \theta(W_{\text{th}} - W) [E_k - H_0] \varphi_c^W(\mathbf{x}). \end{aligned} \quad (2.10)$$

This non-local potential $U(\mathbf{x}, \mathbf{y})$ is energy independent by construction. It is also easy to see that we can make the potential local but energy-dependent. Similar trade-off between non-locality and energy-dependence has been also discussed long time ago in Ref.22) in a different context. Note however that the non-local potential $U(\mathbf{x}, \mathbf{y})$ which satisfied Eq. (2.5) at $W \leq W_{\text{th}}$ is not unique. For example, one may add a term such as $f(\mathbf{x})[1 - P^{W_{\text{th}}}(\mathbf{x}, \mathbf{y})]$ with arbitrary functions $f(\mathbf{x})$ to the non-local potential $U(\mathbf{x}, \mathbf{y})$ without affecting Eq.(2.5) at $W \leq W_{\text{th}}$.

We remark that One may define a non-local potential different from Eq.(2.9) as

$$U^\infty(\mathbf{x}, \mathbf{y}) = \sum_{W \leq \infty} \sum_c [E_k - H_0] P_c^\infty(W; \mathbf{x}, \mathbf{y}), \quad (2.11)$$

which satisfies Eq. (2.5) for all W . This potential, however, becomes long-ranged, due to the presence of inelastic contributions above W_{th} . An extension of the HAL QCD method, which keeps the short-range nature of the potential while inelastic channels open, will be discussed in Sec. 7.

The most general form of the Schrödinger type equation for the NBS wave function has energy-dependent and non-local potential as shown in Ref.16). However, one can always remove its energy-dependence as demonstrated in the above derivation.

2.3. Velocity expansion of the non-local potential

If one knows NBS wave functions φ^W for all $W \leq W_{\text{th}}$, the non-local potential U can be constructed according to Eq. (2.9). In lattice QCD simulations in a finite box, however, only a limited number of wave functions at low energies (ground state and possibly a few low-lying excited states) can be obtained. In such a situation, it is useful to expand the non-local potential in terms of the velocity (derivative) with local coefficient functions;²³⁾

$$U(\mathbf{x}, \mathbf{y}) = V(\mathbf{x}, \nabla) \delta^3(\mathbf{x} - \mathbf{y}). \quad (2.12)$$

In the lowest few orders we have

$$V(\mathbf{r}, \nabla) = \underbrace{V_0(r) + V_\sigma(r) \boldsymbol{\sigma}_1 \cdot \boldsymbol{\sigma}_2 + V_T(r) S_{12}}_{\text{LO}} + \underbrace{V_{\text{LS}}(r) \mathbf{L} \cdot \mathbf{S}}_{\text{NLO}} + O(\nabla^2), \quad (2.13)$$

where $r = |\mathbf{r}|$, $\boldsymbol{\sigma}_i$ is the Pauli-matrix acting on the spin index of the i -th baryon, $\mathbf{S} = (\boldsymbol{\sigma}_1 + \boldsymbol{\sigma}_2)/2$ is the total spin, $\mathbf{L} = \mathbf{r} \times \mathbf{p}$ is the angular momentum, and

$$S_{12} = 3 \frac{(\mathbf{r} \cdot \boldsymbol{\sigma}_1)(\mathbf{r} \cdot \boldsymbol{\sigma}_2)}{r^2} - \boldsymbol{\sigma}_1 \cdot \boldsymbol{\sigma}_2 \quad (2.14)$$

is the tensor operator. Each coefficient function is further decomposed into its flavor components. In the case of nucleons (i.e. $N_f = 2$), we have

$$V_X(r) = V_X^0(r) + V_X^T(r) \boldsymbol{\tau}_1 \cdot \boldsymbol{\tau}_2, \quad X = 0, \sigma, T, \text{LS}, \dots, \quad (2.15)$$

where $\boldsymbol{\tau}_i$ is the Pauli-matrix acting on the flavor index of the i -th nucleon. The form of the velocity expansion (2.13) agrees with the form determined by symmetries.²⁴⁾

At the leading order of the velocity expansion, the local potential is given by

$$V^{\text{LO}}(\mathbf{r}) = V_0(r) + V_\sigma(r) \boldsymbol{\sigma}_1 \cdot \boldsymbol{\sigma}_2 + V_T(r) S_{12}, \quad (2.16)$$

which is obtained from the NBS wave function at one value of W . Since $S_{12} = 0$ for the spin-singlet state, for example, one has

$$V_C(r, S = 0) \equiv V_0(r) - 3V_\sigma(r) = \frac{(E_k - H_0) \varphi^W(\mathbf{r})}{\varphi^W(\mathbf{r})}. \quad (2.17)$$

2.4. Remarks on the “scheme”-dependence of the potential

We emphasize that the potential itself is not a physical observable, and is therefore not a unique quantity in quantum mechanics and in field theory. In fact, the baryon-baryon potential in QCD depends on the choice of the interpolating baryon operator to define the NBS wave function. Among others, the local baryon operator used in HAL QCD method is a most convenient choice, since the reduction formula for composite particles can be derived in a simplest way for this choice.^{25)–27)}

Nevertheless, one may adopt other interpolating operators (such as higher dimensional operators and non-local operators): Particular choice of the baryon operator and associated potential may be considered as a “scheme” to describe physical observables such as the scattering phase shift and the binding energies. The potential, although being “scheme”-dependent, is still useful to understand physical phenomena as we know well in quantum mechanics. The repulsive core of the nucleon-nucleon potential in the coordinate space, which is known to be the best way to summarize the NN scattering phase shift at high energies, is one of such examples.*)

Among different schemes, good convergence of the velocity expansion is an important check of the choice of our present scheme. Such a check can be carried out by examining the W dependence of the lower order potentials. For example, if we have φ^{W_n} for $n = 1, 2, \dots, N$, we can determine the $N - 1$ unknown local functions of the velocity expansion in N different ways. The variation among N different determinations gives an estimate of the size of the higher order terms. Furthermore one of these higher order terms can be determined from φ^{W_n} for $n = 1, 2, \dots, N$. The convergence of the velocity expansion will be investigated explicitly in Sec. 4.

The analysis in this section shows that the use of Schrödinger type equation with non-local potential is justified to describe the BB scattering in QCD. The key quantity is the NBS wave function, whose asymptotic behavior encodes phases of the S-matrix for the BB scattering. If the velocity expansion of the non-local potential is reasonably good at low energies, one can use the LO and NLO potentials to investigate various nuclear many-body problems.

§3. Lattice formulation

We now discuss procedures to extract the NBS wave function from lattice QCD simulations. For this purpose, we consider the correlation function on the lattice defined by

$$F(\mathbf{r}, t - t_0) = \langle 0 | T \{ B(\mathbf{x} + \mathbf{r}, t) B(\mathbf{x}, t) \} \overline{\mathcal{J}}(t_0) | 0 \rangle \quad (3.1)$$

where $\overline{\mathcal{J}}(t_0)$ is a source operator which creates two-baryon states. Inserting a complete set and considering baryon number conservation, we have

$$F(\mathbf{r}, t - t_0) = \langle 0 | T \{ B(\mathbf{x} + \mathbf{r}, t) B(\mathbf{x}, t) \} \sum_{n, s_1, s_2} | 2B, W_n, s_1, s_2 \rangle \langle 2B, W_n, s_1, s_2 | \overline{\mathcal{J}}(t_0) | 0 \rangle$$

*) Although in a different sense of the “scheme”, analogous situation in quantum field theory is the running coupling constant. It is scheme-dependent quantity but is quite useful to understand the high energy processes such as the deep inelastic scattering data.

$$+ \dots = \sum_{n, s_1, s_2} A_{n, s_1, s_2} \varphi^{W_n}(\mathbf{r}) e^{-W_n(t-t_0)} + \dots, \quad (3.2)$$

where $A_{n, s_1, s_2} = \langle 2B, W_n, s_1, s_2 | \bar{\mathcal{J}}(t_0) | 0 \rangle$ and ellipses represent contributions from inelastic states such as $NN\pi$, $NNN\bar{N}$, etc. At large time separation $(t - t_0) \rightarrow \infty$, we obtain

$$\lim_{(t-t_0) \rightarrow \infty} F(\mathbf{r}, t - t_0) = A_0 \varphi^{W_0}(\mathbf{r}) e^{-W_0(t-t_0)} + O(e^{-W_{n \neq 0}(t-t_0)}) \quad (3.3)$$

where W_0 is the lowest energy of BB states. Since the source dependent term A_0 is just a multiplicative constant to the NBS wave function $\varphi^{W_0}(\mathbf{r})$, the potential defined from $\varphi^{W_0}(\mathbf{r})$ is manifestly source-independent. For this extraction of the wave function to work, the ground state saturation for F in Eq. (3.3) must be satisfied by taking large $t - t_0$. In practice, however, F becomes very noisy at large $t - t_0$. In Sec. 3.4, we will discuss more on this point.

3.1. Choice of source operators

We choose the source operator $\bar{\mathcal{J}}$ to fix quantum numbers of $|2B, W, s_1, s_2\rangle$. Since lattice QCD simulations are usually performed on a hyper-cubic lattice, the cubic transformation group $SO(3, \mathbf{Z})$ instead of $SO(3, \mathbf{R})$ is considered as the symmetry of 3-dimensional space. Therefore the quantum number is classified in terms of the irreducible representation of $SO(3, \mathbf{Z})$, which is denoted by A_1, A_2, E, T_1 and T_2 whose dimensions are 1, 1, 2, 3 and 3, respectively. Relation of irreducible representations between $SO(3, \mathbf{Z})$ and $SO(3, \mathbf{R})$ is given in Table I for $L \leq 6$, where L denotes the angular momentum for the irreducible representation of $SO(3, \mathbf{R})$. For example, the source operator $\bar{\mathcal{J}}(t_0)$ in the A_1 representation with positive parity generates states with $L = 0, 4, 6, \dots$ at $t = t_0$, while the operator in the T_1 representation with negative parity produces states with $L = 1, 3, 5, \dots$. For two octet-baryons, the total spin S becomes $1/2 \otimes 1/2 = 1 \oplus 0$, which corresponds to $T_1(S = 1)$ and $A_1(S = 0)$ of $SO(3, \mathbf{Z})$. The total representation J for a two baryon system is thus determined by the product $R_1 \otimes R_2$, where $R_1 = A_1, A_2, E, T_1, T_2$ for the orbital "angular momentum" while $R_2 = A_1, T_1$ for the total spin. In Table II, the product $R_1 \otimes R_2$ is decomposed into the direct sum of irreducible representations.

Table I. The number of each representation of $SO(3, \mathbf{Z})$ which appears in the angular momentum L representation of $SO(3, \mathbf{R})$. $P = (-1)^L$ denotes the eigenvalue under parity transformation.

L	P	A_1	A_2	E	T_1	T_2
0 (S)	+	1	0	0	0	0
1 (P)	-	0	0	0	1	0
2 (D)	+	0	0	1	0	1
3 (F)	-	0	1	0	1	1
4 (G)	+	1	0	1	1	1
5 (H)	-	0	0	1	2	1
6 (I)	+	1	1	1	1	2

Table II. The decomposition of a product of two irreducible representations, $R_1 \otimes R_2$, into irreducible representations in $SO(3, \mathbf{Z})$. Note that $R_1 \otimes R_2 = R_2 \otimes R_1$ by definition.

	A_1	A_2	E	T_1	T_2
A_1	A_1	A_2	E	T_1	T_2
A_2	A_2	A_1	E	T_2	T_1
E	E	E	$A_1 \oplus A_2 \oplus E$	$T_1 \oplus T_2$	$T_1 \oplus T_2$
T_1	T_1	T_2	$T_1 \oplus T_2$	$A_1 \oplus E \oplus T_1 \oplus T_2$	$A_2 \oplus E \oplus T_1 \oplus T_2$
T_2	T_2	T_1	$T_1 \oplus T_2$	$A_2 \oplus E \oplus T_1 \oplus T_2$	$A_1 \oplus E \oplus T_1 \oplus T_2$

We often use the wall source at $t = t_0$ defined by

$$\mathcal{J}^{\text{wall}}(t_0)_{\alpha\beta,fg} = B_{\alpha,f}^{\text{wall}}(t_0)B_{\beta,g}^{\text{wall}}(t_0) \quad (3.4)$$

where $\alpha, \beta = 1, 2$ are upper component of the spinor indices while f, g are flavor indices. Here $B^{\text{wall}}(t_0)$ is obtained by replacing the local quark field $q(x)$ of $B(x)$ by the wall source,

$$q^{\text{wall}}(t_0) \equiv \sum_{\mathbf{x}} q(\mathbf{x}, t_0) \quad (3.5)$$

with the Coulomb gauge fixing at $t = t_0$. Note that this gauge-dependence of the source operator disappears for the potential. All states created by the wall source have zero total momentum. Among them the state with zero relative momentum has the largest magnitude. A reason for employing the wall source here is that the ground state saturation for the potential at long distance is better achieved for the wall source than for other sources.

Let us consider the case of the two nucleons. The source operator $\bar{\mathcal{J}}^{\text{wall}}(t_0)$ has zero orbital angular momentum at $t = t_0$, which corresponds to the A_1 representation with positive parity. Therefore, the total angular momentum can be fixed by using the spin recoupling matrix $M^{(S,S_z)}$, e.g., $M^{(S=0,S_z=0)} \equiv \sigma_2/\sqrt{2}$ and $M^{(S=1,S_z=m)} \equiv (\sigma_2\sigma_m)/\sqrt{2}$ for $m = 0, \pm 1$ as

$$\mathcal{J}(t_0; J^{P=+}, J_z = m, I) = M_{\beta\alpha}^{(S)} \mathcal{J}^{\text{wall}}(t_0)_{\alpha\beta,fg}. \quad (3.6)$$

Here $P = \pm$ is the parity and $I = 1, 0$ is the total isospin of the system. Since the nucleon is a fermion, exchange of the nucleon operators in the source should give a minus sign. This fact fixes the total isospin given the total spin: $(S, I) = (0, 1)$ or $(1, 0)$. (Note that $S, I = 0$ are antisymmetric while $S, I = 1$ are symmetric under the exchange.) Since $A_1^+ \otimes A_1(S = 0) = A_1^+$ and $A_1^+ \otimes T_1(S = 1) = T_1^+$, the state with either $(J^P, I) = (A_1^+, 1)$ for the spin-singlet or $(J^P, I) = (T_1^+, 0)$ for the spin-triplet is created at $t = t_0$ by the corresponding source operator. The NBS wave function extracted at $t > t_0$ has the same quantum numbers (J^P, I) as they are conserved under QCD interactions. In addition the total spin S is conserved at $t > t_0$ for the two nucleon system with equal up and down quark masses: Under the exchange of the two particles, the constraint $(-1)^{S+1+I+1}P = -1$ must be satisfied due to the fermionic nature of the nucleon. Also, the parity P and the isospin I are conserved in this system. Therefore S is conserved. However, L is not conserved in general.

While the state with $(J^P, I) = (A_1^+, 1)$ always has $L = A_1^+$ even at $t > t_0$, the one with $(J^P, I) = (T_1^+, 0)$ has both $L = A_1^+$ and $L = E^+, T_2^+$ components^{*)} at $t > t_0$, which corresponds to $L = 0$ and $L = 2$ in $SO(3, \mathbf{R})$, respectively. Note that J and L are used to represent the total and orbital quantum numbers respectively for $SO(3, \mathbf{Z})$ as well as for $SO(3, \mathbf{R})$.

The orbital angular momentum L of the NBS wave function for NN can be fixed to a particular value by the projection operator $P^{(L)}$ as

$$\varphi^W(\mathbf{r}; J^P, I, L, S) = P^{(L)} P^{(S)} \varphi^W(\mathbf{r}; J^P, I) \quad (3.7)$$

where $\varphi^W(\mathbf{r}; J^P, I)$ is extracted from

$$\begin{aligned} F(\mathbf{r}, t - t_0; J^P, I) &\simeq A(J^P, I) \varphi^W(\mathbf{r}; J^P, I) e^{-W(t-t_0)}, \\ A(J^P, I) &= \langle 2B, W | \bar{\mathcal{J}}(t_0; J^P, I) | 0 \rangle \end{aligned} \quad (3.8)$$

for large $t-t_0$. The total spin projection operator is $(P^{(S=0)})_{\alpha\beta; \alpha'\beta'} \equiv \frac{1}{2}(\sigma_2)_{\alpha\beta}(\sigma_2)_{\beta'\alpha'}$ for spin-singlet and $P^{(S=1)} \equiv \mathbb{I} - P^{(S=0)}$ for spin-triplet, but this is redundant since the total spin S , already fixed by the source, is conserved as mentioned before. The projection operator $P^{(L)}$ of the orbital angular momentum for an arbitrary function $\varphi(\mathbf{r})$ is defined in general by

$$P^{(L)} \varphi^W(\mathbf{r}) \equiv \frac{d_L}{24} \sum_{g \in SO(3, \mathbf{Z})} \chi^L(g)^* \varphi^W(g^{-1} \cdot \mathbf{r}) \quad (3.9)$$

for $L = A_1, A_2, E, T_1, T_2$, where χ^L denotes the character of the representation L in $SO(3, \mathbf{Z})$, $*$ is its complex conjugate, g is one of 24 elements in $SO(3, \mathbf{Z})$ and d_L is the dimension of L .

3.2. Leading order NN potential: spin-singlet case

We present the procedure to determine potentials at the leading order(LO):

$$V^{\text{LO}}(\mathbf{r}) = V_0(r) + V_\sigma(r)(\boldsymbol{\sigma}_1 \cdot \boldsymbol{\sigma}_2) + V_T(r)S_{12}. \quad (3.10)$$

Since $S_{12} = 0$ and $\boldsymbol{\sigma}_1 \cdot \boldsymbol{\sigma}_2 = -3$ for the spin-singlet case, the LO central potential for the spin-singlet case is extracted from the $(J^P, I) = (A_1^+, 1)$ state as

$$V_C(r)^{(S,I)=(0,1)} \equiv V_0^{I=1}(r) - 3V_\sigma^{I=1}(r) = \frac{[E_k - H_0] \varphi^W(\mathbf{r}; A_1^+, I=1, L=A_1, S=0)}{\varphi^W(\mathbf{r}; A_1^+, I=1, L=A_1, S=0)}, \quad (3.11)$$

where $V_X^{I=1} = V_X^0 + V_X^T$ in isospin space. The potential $V_C(\mathbf{r})^{(S,I)=(0,1)}$ in the above is often referred to as the central potential for the 1S_0 state, where the notation $^{2S+1}L_J$ represents the orbital angular momentum L (see Table I), the total spin S and the total angular momentum J of $\mathbf{J} = \mathbf{L} + \mathbf{S}$. It is noted, however, that in the leading order of the velocity expansion, the potential does not depend on the

^{*)} This can be seen from Table II for $R_2 = T_1$ (spin-triplet), which also tells us the existence of $L = T_1^+$ component in addition. The extra component is expected to be small since it appears as a consequence of the violation of $SO(3, \mathbf{R})$ on the hyper-cubic lattice.

quantum number of the state $J = L = A_1$. Moreover the A_1 state may contain $L = 4, 6, \dots$ components other than $L = 0$, though the $L = 0$ component may dominate. Therefore it is more precise to refer to $V_C(\mathbf{r})^{(S,I)=(0,1)}$ as the spin-singlet (isospin-triplet) central potential determined from the state with $J = L = A_1$. A possible difference of spin-singlet central potentials between this determination and others such as the one determined from $J = L = E$ gives an estimate for contributions from higher order terms in the velocity expansion.

3.3. Leading order potential: spin-triplet case

Both the tensor potential V_T and central potential V_C appear in the LO for the spin-triplet case. Let us consider the determination from $(J^P, I) = (T_1^+, 0)$ state. The Schrödinger equation for this state becomes

$$\left[H_0 + V_C(r)^{(S,I)} + V_T(r)S_{12} \right] \varphi^W(\mathbf{r}; J^P = T_1^+, I) = E_k \varphi^W(\mathbf{r}; J^P = T_1^+, I) \quad (3.12)$$

with $(S, I) = (1, 0)$, where the spin-triplet central potential is given by

$$V_C(r)^{(1,0)} \equiv V_0^{I=0}(r) + V_\sigma^{I=0}(r), \quad V_X^{I=0} = V_X^0 - 3V_X^\tau. \quad (3.13)$$

We separate the Schrödinger equation Eq. (3.12) into the A_1 and non- A_1 components by using projection operators $\mathcal{P} \equiv P^{(A_1)}$ and $\mathcal{Q} \equiv \mathbb{I} - \mathcal{P}$ as

$$\begin{aligned} (V_C(r)^{(1,0)} - E_k)\mathcal{P}\varphi^W(\mathbf{r}) + V_T(r)\mathcal{P}S_{12}\varphi^W(\mathbf{r}) &= -H_0\mathcal{P}\varphi^W(\mathbf{r}) \\ (V_C(r)^{(1,0)} - E_k)\mathcal{Q}\varphi^W(\mathbf{r}) + V_T(r)\mathcal{Q}S_{12}\varphi^W(\mathbf{r}) &= -H_0\mathcal{Q}\varphi^W(\mathbf{r}). \end{aligned} \quad (3.14)$$

Note that \mathcal{P} and \mathcal{Q} commute with H_0 , $V_C(r)$ and $V_T(r)$, whereas they do not commute with S_{12} . Non- A_1 component receives contributions from E , T_1 and T_2 , among which only E and T_2 contribute to the D-wave. Since the contribution from T_1 component turns out to be negligible in the numerical simulation, the non- A_1 component is dominated by D-wave contributions.

Using these projections, V_C and V_T can be extracted as

$$\begin{aligned} V_C(r)^{(1,0)} &= E_k - \frac{1}{\Delta(\mathbf{r})} ([\mathcal{Q}S_{12}\varphi^W]_{\alpha\beta}(\mathbf{r})H_0[\mathcal{P}\varphi^W]_{\alpha\beta}(\mathbf{r}) \\ &\quad - [\mathcal{P}S_{12}\varphi^W]_{\alpha\beta}(\mathbf{r})H_0[\mathcal{Q}\varphi^W]_{\alpha\beta}(\mathbf{r})) \end{aligned} \quad (3.15)$$

$$V_T(r) = \frac{1}{\Delta(\mathbf{r})} ([\mathcal{Q}\varphi^W]_{\alpha\beta}(\mathbf{r})H_0[\mathcal{P}\varphi^W]_{\alpha\beta}(\mathbf{r}) - [\mathcal{P}\varphi^W]_{\alpha\beta}(\mathbf{r})H_0[\mathcal{Q}\varphi^W]_{\alpha\beta}(\mathbf{r})) \quad (3.16)$$

$$\Delta(\mathbf{r}) \equiv [\mathcal{Q}S_{12}\varphi^W]_{\alpha\beta}(\mathbf{r})[\mathcal{P}\varphi^W]_{\alpha\beta}(\mathbf{r}) - [\mathcal{P}S_{12}\varphi^W]_{\alpha\beta}(\mathbf{r})[\mathcal{Q}\varphi^W]_{\alpha\beta}(\mathbf{r}). \quad (3.17)$$

In numerical simulations, $(\alpha, \beta) = (2, 1)$ in $J_z = 0$ state is mainly employed.

One may focus only on the A_1 component of the wave function and define so-called the effective central potential for the spin-triplet (isospin-singlet), often used in nuclear physics:

$$V_C^{\text{eff}}(r)^{(1,0)} = \frac{[E_k - H_0]\mathcal{P}\varphi_{\alpha\beta}^W(\mathbf{r})}{\mathcal{P}\varphi_{\alpha\beta}^W(\mathbf{r})}. \quad (3.18)$$

The effect of V_T , which leads to a transition from the A_1 component to the non- A_1 component of the wave-function, is implicitly included in this effective central potential: For small V_T , the difference between V_C and V_C^{eff} is $O(V_T^2)$ as the second order perturbation tells us.

3.4. Time-dependent HAL QCD method

One of the practical difficulties to extract the NBS wave function and the potential from the correlation function Eq.(3.1) is to achieve the ground state saturation in numerical simulations at large but finite $t-t_0$ with reasonably small statistical errors. While the stability of the potential against $t-t_0$ has been confirmed within statistical errors in numerical simulations,^{9),18)} the determination of W for the ground state suffers from systematic errors due to contaminations of possible excited states. There exist three different methods to determine W . The most well-known method is to determine W from the $t-t_0$ dependence of the correlation function Eq.(3.1) summed over \mathbf{r} to pick up the zero momentum state. On the other hand, one may determine \mathbf{k}^2 of W by fitting the \mathbf{r} dependence of the NBS wave function with its expected asymptotic behavior at large r or by reading off the constant shift of the Laplacian part of the potential from zero at large r . Although the latter two methods usually give consistent results within statistical errors, the first method sometimes leads to a result different from those determined by the latter two at the value of $t-t_0$ employed in numerical simulations. Although, in principle, the increase of $t-t_0$ is needed in order to see an agreement among three methods, it is difficult in practice due to larger statistical errors at large $t-t_0$.

The problem above is common in various applications of lattice QCD. Fortunately, the original HAL QCD method can be improved to overcome this difficulty as follows. Let us consider the normalized correlation function defined from Eq.(3.1) as

$$R(\mathbf{r}, t) \equiv \frac{F(\mathbf{r}, t)}{e^{-2m_B t}} = \sum_n A_n \varphi^{W_n}(\mathbf{r}) \exp(-t \Delta W_n) + O(e^{-\Delta W_{\text{th}} t}), \quad (3.19)$$

where $\Delta W_n = W_n - 2m_B$ and $\Delta W_{\text{th}} = W_{\text{th}} - 2m_B = m_M$. By neglecting the inelastic contributions above the meson production threshold, represented by $O(e^{-\Delta W_{\text{th}} t})$, for large enough t^* , non-relativistic approximation $W_n - 2m_B \simeq k_n^2/m_B$ leads us to

$$\begin{aligned} R(\mathbf{r}, t) &\simeq \sum_n A_n \varphi^{W_n}(\mathbf{r}) \exp\left(-t \frac{k_n^2}{m_B}\right) = e^{-t(H_0+U)} \sum_n A_n \varphi^{W_n}(\mathbf{r}) \\ &= e^{-t(H_0+U)} R(\mathbf{r}, t=0), \end{aligned} \quad (3.20)$$

where the Schrödinger equation Eq. (2.5), the defining relation of the non-local potential U , is used to replace $e^{-tk_n^2/m_B}$ by $e^{-t(H_0+U)}$. By applying a time derivative on both side, we have the time-dependent Schrödinger equation in imaginary time

$$\left(-\frac{\partial}{\partial t} - H_0\right) R(\mathbf{r}, t) \simeq \int d^3\mathbf{r}' U(\mathbf{r}, \mathbf{r}') R(\mathbf{r}', t). \quad (3.21)$$

^{*)} This limitation for t can be removed if the coupled channel potentials are introduced as in Sec. 7.

Now the velocity expansion of the non-local potential leads us to the formula of the leading order potential

$$V^{\text{LO}}(\mathbf{r}) = -\frac{(\partial/\partial t)R(\mathbf{r}, t)}{R(\mathbf{r}, t)} - \frac{H_0 R(\mathbf{r}, t)}{R(\mathbf{r}, t)}. \quad (3.22)$$

Once the ground state saturation is achieved in $R(\mathbf{r}, t)$, Eq.(3.22) reduces to Eq.(2.17), for example for the spin-singlet case. Indeed, in this case, $-\partial/\partial t$ is safely replaced by the non-relativistic energy E_k of the ground state under the non-relativistic approximation.

The non-relativistic formula for $V^{\text{LO}}(r)$ above can be generalized to the case that masses of two particles are different by the replacement, $R(\mathbf{r}, t) = F(\mathbf{r}, t)/e^{-(m_A+m_B)t}$. Note also that the potential extracted in this method automatically satisfies $V^{\text{LO}}(r \rightarrow 0) \rightarrow 0$ without constant shift. This property can be used to check whether this extraction works correctly or not.

The non-relativistic approximation used to derive Eq.(3.19) can be removed by using the second order derivative in t ;

$$\left(\frac{1}{4m_B} \frac{\partial^2}{\partial t^2} - \frac{\partial}{\partial t} - H_0 \right) R(\mathbf{r}, t) = \int d^3 \mathbf{r}' U(\mathbf{r}, \mathbf{r}') R(\mathbf{r}', t), \quad (3.23)$$

which leads to

$$V^{\text{LO}}(\mathbf{r}) = \frac{1}{4m_B} \frac{(\partial/\partial t)^2 R(\mathbf{r}, t)}{R(\mathbf{r}, t)} - \frac{(\partial/\partial t)R(\mathbf{r}, t)}{R(\mathbf{r}, t)} - \frac{H_0 R(\mathbf{r}, t)}{R(\mathbf{r}, t)}. \quad (3.24)$$

Here we have assumed that the inelastic contributions are negligibly small and that the two particles have the same mass. Since t is discrete on the lattice, the t derivatives has to be carefully performed. One has to employ the numerical derivative scheme which reduces statistical as well as systematic errors of $V^{\text{LO}}(\mathbf{r})$.

One can generalize Eq.(3.19) to the correlation function with two relative coordinates \mathbf{x} and \mathbf{y} ;

$$R(\mathbf{x}, \mathbf{y}, t) = \frac{1}{e^{-2m_B t}} \int d^3 \mathbf{x}_1 d^3 \mathbf{y}_1 \langle 0 | T \{ B(\mathbf{x}_1 + \mathbf{x}, t) B(\mathbf{x}_1, t) \bar{B}(\mathbf{y}_1 + \mathbf{y}, 0) \bar{B}(\mathbf{y}_1, 0) \} | 0 \rangle, \quad (3.25)$$

which leads to

$$\left(\frac{1}{4m_B} \frac{\partial^2}{\partial t^2} - \frac{\partial}{\partial t} - H_0 \right) R(\mathbf{x}, \mathbf{y}, t) = \int d^3 \mathbf{z} U(\mathbf{x}, \mathbf{z}) R(\mathbf{z}, \mathbf{y}, t). \quad (3.26)$$

Then, we obtain the non-local potential as

$$U(\mathbf{x}, \mathbf{y}) = \int d^3 \mathbf{z} \left(\frac{1}{4m_B} \frac{\partial^2}{\partial t^2} - \frac{\partial}{\partial t} - H_0 \right) R(\mathbf{x}, \mathbf{z}, t) \cdot \tilde{R}^{-1}(\mathbf{z}, \mathbf{y}, t), \quad (3.27)$$

where $\tilde{R}^{-1}(\mathbf{x}, \mathbf{y}, t)$ is an ‘‘truncated’’ inverse of the Hermitian operator $R(\mathbf{x}, \mathbf{y}, t)$,

$$\tilde{R}^{-1}(\mathbf{x}, \mathbf{y}, t) = \sum_{\lambda_n \neq 0} \frac{1}{\lambda_n(t)} v_n(\mathbf{x}, t) v_n^\dagger(\mathbf{y}, t) \quad (3.28)$$

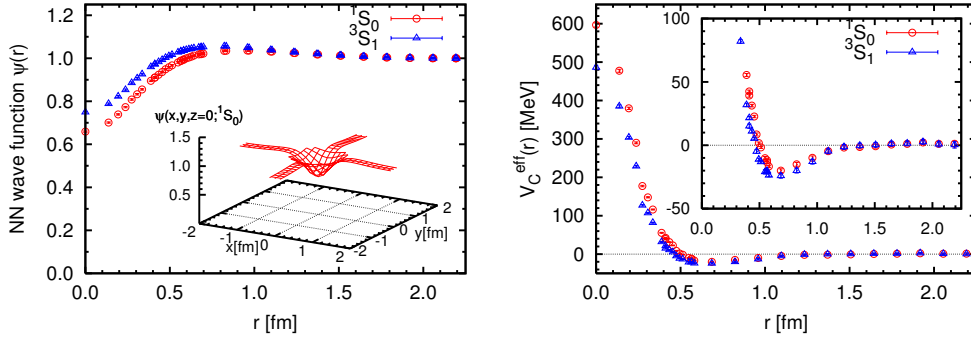


Fig. 2. (Left) The NN wave function for the spin-singlet and spin-triplet channels in the orbital A_1^+ representation at $m_\pi \simeq 529$ MeV and $a \simeq 0.137$ fm in quenched QCD. The insert is a three-dimensional plot of the spin-singlet wave function $\varphi^W(x, y, z = 0)$. (Right) The NN (effective) central potential for the spin-singlet (spin-triplet) channel determined from the orbital A_1^+ wave function. Both figures are taken from Ref. 18).

with $\lambda_n(t)$ and $v_n(\mathbf{x}, t)$ being the eigenvalues and corresponding eigenvectors of $R(\mathbf{x}, \mathbf{y}, t)$, respectively. Note that zero eigenvalues are removed in the above summation. Suppose we introduce a modified potential as

$$\hat{U}(\mathbf{x}, \mathbf{y}) = U(\mathbf{x}, \mathbf{y}) + \sum_{\lambda_n=0} c_n v_n(\mathbf{x}, t) v_n^\dagger(\mathbf{y}, t). \quad (3.29)$$

Then it satisfies the same Schrödinger equation for all possible values of c_n , the non-local potential is not unique as discussed before.

§4. NN potential from lattice QCD

4.1. Central potential in quenched QCD

Let us first show results in the quenched QCD, where creations and annihilations of virtual quark-antiquark pairs are neglected: The standard plaquette gauge action is employed on a 32^4 lattice at the bare gauge coupling constant $\beta = 6/g^2 = 5.7$. This corresponds to the lattice spacing $a \simeq 0.137$ fm ($1/a = 1.44(2)$ GeV), determined from the ρ meson mass in the chiral limit, and the physical size of the lattice $L \simeq 4.4$ fm.⁹⁾ As for the quark action, the standard Wilson fermion action is used at three different values of the quark mass corresponding to the pion mass $m_\pi \simeq 731, 529, 380$ MeV and the nucleon mass $m_N \simeq 1560, 1330, 1200$ MeV, respectively.

Fig. 2(Left) shows the NBS wave functions for the spin-singlet and the spin-triplet channels in the orbital A_1 representation at $m_\pi \simeq 529$ MeV. These wave functions are normalized to be 1 at the largest spatial point $r \simeq 2.2$ fm. The central potential in the spin-singlet channel and the effective central potential in the spin-triplet channel extracted from the wave functions at $m_\pi \simeq 529$ MeV are shown in Fig. 2(Right). These potentials reproduce the qualitative features of the phenomenological NN potentials, namely the repulsive core at short distance sur-

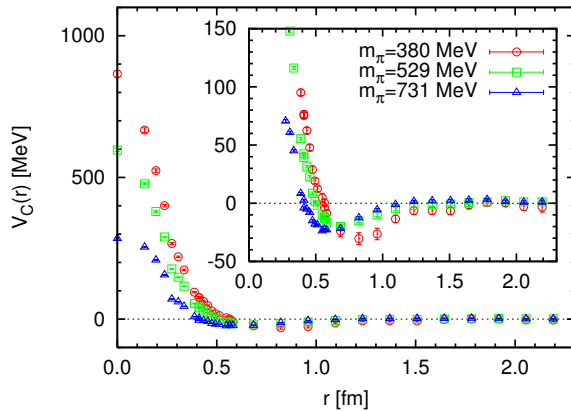


Fig. 3. The central potentials for the spin-singlet channel from the orbital A_1^+ representation at three different pion masses in quenched QCD. Taken from Ref. 18).

rounded by the attractive well at medium and long distances. From this figure one observes that the interaction range of the potential is smaller than 1.5 fm, showing that the box size $L \simeq 4.4$ fm is large enough for the potential. Labels 1S_0 and 3S_1 of the potentials in the figure represent the fact that potentials are determined from A_1 wave functions, which are dominated by the S -wave component. Note here that the lattice artifacts are expected to be large for potentials (as well as wave functions) at short distance such that $r \simeq O(a)$. Therefore our results at short distance should be considered to be qualitative, not quantitative, and this caution should be applied to all of our results in this paper otherwise stated. The continuum extrapolation is necessary to predict short distance behaviors of potentials quantitatively. Indeed, BB potentials in the continuum limit are shown to diverge as $r \rightarrow 0$.^{28),29)}

In Fig.3, NN central potentials in the spin-singlet channel are shown for three different pion masses. The repulsion at short distance and the attraction at medium distance are simultaneously enhanced as the pion mass decreases.

4.2. Tensor potential in quenched QCD

In Fig. 4(Left), we show the A_1 and non- A_1 components of the NBS wave function obtained from the $J^P = T_1^+$ (and $J_z = S_z = 0$) states at $m_\pi \simeq 529$ MeV. The non- A_1 wave function is multivalued as a function of r due to its angular dependence. For example, the $(\alpha, \beta) = (2, 1)$ component of the $L = 2$ part of the non- A_1 wave function is proportional to the spherical harmonics $Y_{20}(\theta, \phi) \propto 3 \cos^2 \theta - 1$. Fig. 4(Right) shows the non- A_1 component divided by $Y_{20}(\theta, \phi)$. The non- A_1 wave function seems to be dominated by the D ($L = 2$) state, since its multivaluedness is mostly absorbed to $Y_{20}(\theta, \phi)$. Fig. 5 (Left) shows the central potential $V_C(r)^{(1,0)}$ and tensor potential $V_T(r)$, together with the effective central potential $V_C^{\text{eff}}(r)^{(1,0)}$, at the leading order of the velocity expansion as given in Eqs. (3·15), (3·16) and (3·18), respectively.

Note that $V_C^{\text{eff}}(r)$ contains the effect of $V_T(r)$ implicitly as higher order effects through processes such as $^3S_1 \rightarrow ^3D_1 \rightarrow ^3S_1$. At the physical pion mass, $V_C^{\text{eff}}(r)$ is

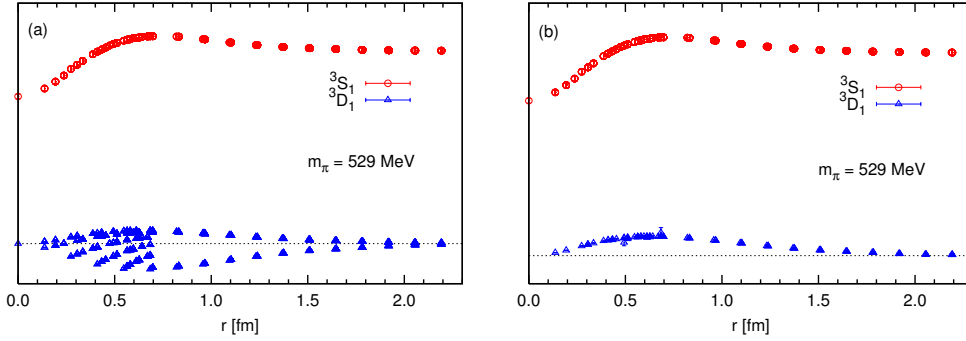


Fig. 4. (Left) $(\alpha, \beta) = (2, 1)$ components of the orbital A_1^+ and non- A_1^+ wave functions from $J^P = T_1^+$ (and $J_z = S_z = 0$) states at $m_\pi \simeq 529$ MeV. (Right) The same wave functions but the spherical harmonics components are removed from the non- A_1^+ part. Taken from Ref. 18).

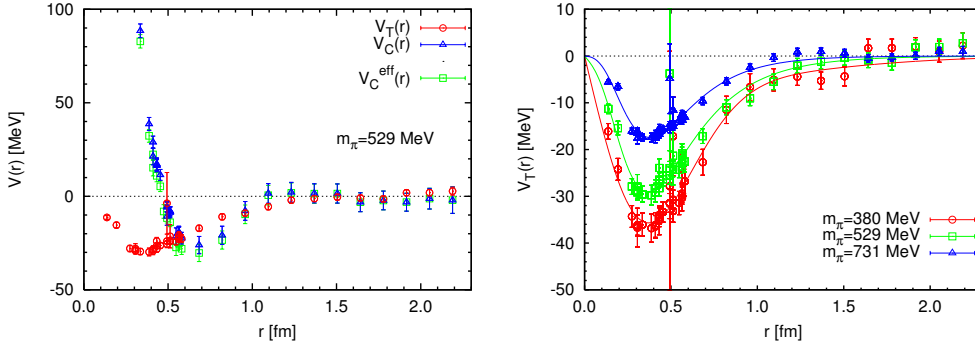


Fig. 5. (Left) The central potential $V_C(r)^{(1,0)}$ and the tensor potential $V_T(r)$ obtained from the $J^P = T_1^+$ NBS wave function, together with the effective central potential $V_C^{\text{eff}}(r)^{(1,0)}$, at $m_\pi \simeq 529$ MeV. (Right) Pion mass dependence of the tensor potential. The lines are the four-parameter fit using one-pion-exchange + one-rho-exchange with Gaussian form factor. Taken from Ref. 18).

expected to gain sufficient attraction from the tensor potential, which leads to the appearance of a bound deuteron in the spin-triplet (and flavor-singlet) channel while an absence of the bound dineutron in the spin-singlet (and flavor-triplet) channel. The difference between $V_C(r)^{(1,0)}$ and $V_C^{\text{eff}}(r)$ in Fig. 5 (Left) is still small in this quenched simulation due to relatively large pion mass.

The tensor potential in Fig. 5 (Left) is negative for the whole range of r within statistical errors and has a minimum around 0.4 fm. If the tensor potential receives a significant contribution from one-pion exchange as expected from the meson theory, $V_T(r)$ is rather sensitive to the change of the pion mass. As shown in Fig. 5 (Right), it is indeed the case: Attraction of $V_T(r)$ is substantially enhanced as the pion mass decreases.

The central and tensor potentials in lattice QCD are given at discrete data points. For practical applications to nuclear physics, however, it is more convenient to parameterize the lattice results by known functions. Such a fit for $V_T(r)$ is given

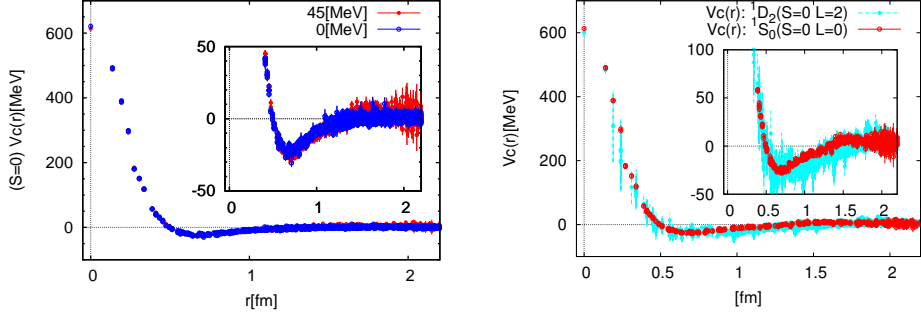


Fig. 6. (Left) The spin-singlet central potential $V_C(r)^{(0,1)}$ obtained from the orbital A_1^+ channel at $E \simeq 45$ MeV (red solid circles) and at $E \simeq 0$ MeV (blue open circles) in quenched QCD at $m_\pi \simeq 529$ MeV. (Right) The same potentials at $E \simeq 45$ MeV, obtained from the orbital A_1^+ representation (red open circles) and from the T_2^+ representation (cray solid circles). Taken from Ref. 33).

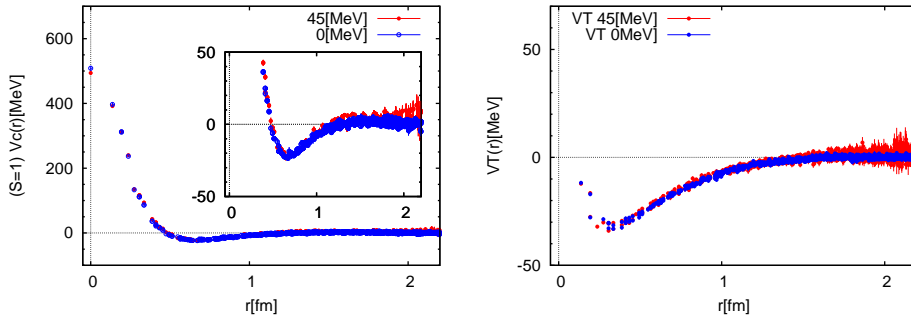


Fig. 7. (Left) The spin-triplet central potential $V_C(r)^{(1,0)}$ obtained from the orbital $A_1^+ - T_2^+$ coupled channel in quenched QCD at $m_\pi \simeq 529$ MeV. (Right) The tensor potential $V_T(r)$ from the orbital $A_1^+ - T_2^+$ coupled channel. For these two figures, symbols are same as in Fig. 6(Left). Taken from Ref. 33).

by the form of one-pion-exchange + one-rho-exchange with Gaussian form factors as

$$\begin{aligned}
 V_T(r) = & b_1(1 - e^{-b_2 r^2})^2 \left(1 + \frac{3}{m_\rho r} + \frac{3}{(m_\rho r)^2} \right) \frac{e^{-m_\rho r}}{r} \\
 & + b_3(1 - e^{-b_4 r^2})^2 \left(1 + \frac{3}{m_\pi r} + \frac{3}{(m_\pi r)^2} \right) \frac{e^{-m_\pi r}}{r}, \quad (4.1)
 \end{aligned}$$

where $b_{1,2,3,4}$ are the fitting parameters while m_π (m_ρ) is taken to be the pion mass (the rho meson mass) calculated at each pion mass. The fit line for each pion mass is drawn in Fig. 5 (Right). It may be worth mentioning that the pion-nucleon coupling constant extracted from the parameter b_3 in the case of the lightest pion mass ($m_\pi = 380$ MeV) gives $g_{\pi N}^2/(4\pi) = 12.1(2.7)$, which is encouragingly close to the empirical value.

4.3. Validity of velocity expansion in quenched QCD

The potentials so far are derived in the leading order of the velocity expansion. It is therefore important to investigate the convergence of the velocity expansion. If the non-locality of the NN potentials were absent, the leading order approximation for the potentials would give exact results at all energies below the inelastic threshold. The non-locality of the potentials therefore becomes manifest in the energy dependence of the potentials.

To study the energy dependence, the leading order local potentials at $E \simeq 45$ MeV, realized by anti-periodic boundary conditions in the spatial directions, are calculated in quenched QCD at $m_\pi \simeq 529$ MeV and $L \simeq 4.4$ fm.^{30)–33)} In this calculation, four types of momentum-wall sources, defined by

$$q(t_0; f) \equiv \sum_{\mathbf{x}} q(\mathbf{x}, t_0) f(\mathbf{x}) \quad (4.2)$$

are employed, where $f(\mathbf{x}) = \cos((\pm x \pm y + z)\pi/L)$. Note that $f(\mathbf{x}) = 1$ corresponds to the wall source used in the periodic boundary condition. These momentum-wall sources induce $L = T_2^+$ as well as $L = A_1^+$ states.

In Fig. 6(Left), the spin-singlet potential $V_C(r)^{(S,I)=(0,1)}$ obtained from the $L = A_1^+$ state at $E \simeq 45$ MeV (red circles) is compared with that at $E \simeq 0$ MeV (blue circles), while a comparison is made in Fig. 7 for the spin-triplet potentials, $V_C(r)^{(S,I)=(1,0)}$ (left) and $V_T(r)$ (right). Good agreements between results at two energies indicate that higher order contributions are rather small in this energy interval. In other words, these local potentials obtained at $E \simeq 0$ MeV can be safely used to describe the NN scattering phase shift in the range between $E = 0$ MeV and $E = 45$ MeV at this pion mass in quenched QCD.

Non-locality of the potential may become manifest also in its angular momentum dependence, since the orbital angular momentum $L = \mathbf{r} \times \mathbf{p}$ contains a derivative. In Fig. 6 (Right), the spin-singlet potential $V_C(r)^{(S,I)=(0,1)}$ obtained from the $L = T_2^+$ state, whose main component has $L = 2$, is compared to the one from the $L = A_1^+$ state, whose main component has $L = 0$. In this comparison, local potentials are determined at the same energy, $E \simeq 45$ MeV, but different orbital angular momentum. Although the statistical errors are rather large in the case of $L = T_2^+$, a good agreement between the two is again observed, suggesting that the L dependence of the potential is small at least for the spin-singlet case.

By these comparisons, it is observed that both energy and orbital angular momentum dependencies for local potentials are very weak within statistical errors. We therefore conclude that contributions from higher order terms in the velocity expansion are small and that the LO local potentials in the expansion obtained at $E \simeq 0$ MeV and $L = 0$ are good approximations for the non-local potentials at least up to the energy $E \simeq 45$ MeV and orbital angular momentum $L = 2$.

4.4. Central potential in full QCD

Needless to say, it is important to carry out calculations of NN potentials in full QCD on larger volumes at lighter pion masses. The PACS-CS collaboration is performing $2 + 1$ flavor QCD simulations, which cover the physical pion mass.^{34), 35)}

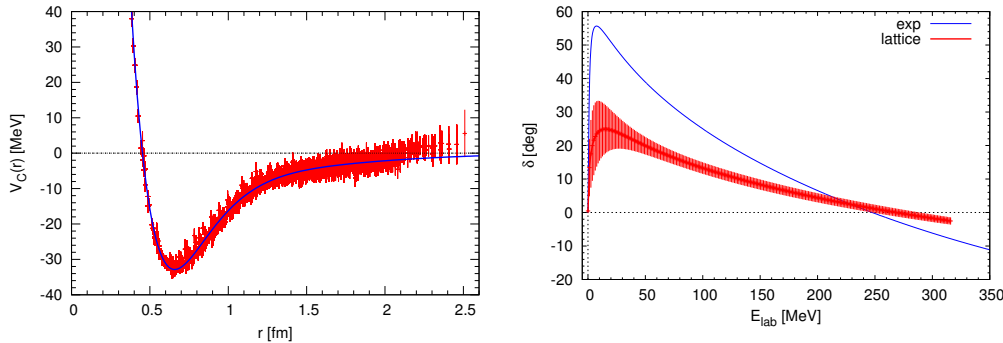


Fig. 8. (left) The multi-Gaussian fit of the central potential $V_C(r)$ with $N_{\text{Gauss}} = 5$. (right) The scattering phase in 1S_0 channel in the laboratory frame obtained from the lattice NN potential, together with experimental data (38).

Gauge configurations are generated with the Iwasaki gauge action and $O(a)$ -improved Wilson quark action on a $32^3 \times 64$ lattice. The lattice spacing a is determined from m_π , m_K and m_Ω as $a \simeq 0.089$ fm, leading to $L \simeq 2.9$ fm. Three ensembles of gauge configurations are used to calculate NN potentials at $(m_\pi, m_N) \simeq (701 \text{ MeV}, 1583 \text{ MeV})$, $(570 \text{ MeV}, 1412 \text{ MeV})$ and $(411 \text{ MeV}, 1215 \text{ MeV})$ ³⁶⁾. To overcome a difficulty to achieve ground state saturations in full QCD simulations, the time-dependent HAL QCD method in Sec. 3.4 is employed.³⁷⁾

Fig. 8(Left) shows the spin-singlet NN central potential $V_C(r)$ obtained at $E \simeq 0$ from the PACS-CS configurations with $m_\pi \simeq 701$ MeV and $m_N \simeq 1583$ MeV. This central potential $V_C(r)$ is fitted with multi-Gaussian function that $g(r) = \sum_{n=1}^{N_{\text{Gauss}}} V_n \exp(-\nu_n r^2)$ with fit parameters V_n and $\nu_n (> 0)$. A solid line in the figure represents a fit result with $N_{\text{Gauss}} = 5$.

We solve the Schrödinger equation in 1S_0 channel with this fitted potential $V_C(r)$, in order to calculate the scattering phase shift. Fig. 8(Right) shows the scattering phase $\delta(k)$ in the laboratory frame, together with the experimental data³⁸⁾ for a comparison. A qualitative feature of the experimental data is well reproduced by the lattice potential, though the strength is weaker, most likely due to the heavier pion mass, $m_\pi \simeq 701$ MeV. The scattering length obtained from the derivative of the phase shift at $k = 0$ becomes $a(^1S_0) = \lim_{k \rightarrow 0} \tan \delta(k)/k = 1.6(1.1)$ fm, which is compared to the experimental value $a^{\text{exp}}(^1S_0) \simeq 20$ fm.

4.5. Nuclear force in odd parity sector and the spin-orbit force in full QCD

In this subsection, we consider the potentials in odd parity sectors. Together with the nuclear forces in even parity sectors, the information on odd parity sectors is necessary in studying many-nucleon systems with Schrödinger equations. In particular, we are interested in the spin-orbit (LS) force, which gives rise to a part of the spin-orbit coupling in the average single-particle potential of nuclei. It is also expected to induce superfluidity in neutron stars by providing an attraction between two neutrons in 3P_2 channel.¹³⁾

The LS force appear at NLO of the derivative expansion as

$$\left[H_0 + V_C(r)^{(S,I)} + V_T(r)S_{12} + V_{LS}(r)\mathbf{L} \cdot \mathbf{S} \right] \varphi^W(\mathbf{r}; J^-, I) = E_k \varphi^W(\mathbf{r}; J^-, I) \quad (4.3)$$

To obtain three unknown potentials, V_C , V_T and V_{LS} , we need three independent NBS wave functions. We therefore generalize the two-nucleon source for odd parity sectors, by imposing a momentum on the composite nucleon fields as

$$\mathcal{J}_{\alpha\beta}(t_0; f^{(i)}) \equiv N_\alpha(t_0; f^{(i)})N_\beta(t_0; f^{(i)*}) \quad \text{for } i = \pm 1, \pm 2, \pm 3, \quad (4.4)$$

where N denotes a composite nucleon source field carrying a momentum,

$$N_\alpha(t_0; f^{(i)}) \equiv \sum_{\mathbf{x}_1, \mathbf{x}_2, \mathbf{x}_3} \epsilon_{abc} (u_a^T(\mathbf{x}_1) C \gamma_5 d_b(\mathbf{x}_2)) q_{c,\alpha}(\mathbf{x}_3) f^{(i)}(\mathbf{x}_3), \quad (4.5)$$

with $f^{(\pm j)}(\mathbf{x}) = \exp[\pm 2\pi i x_j / L]$. The star “*” in the r.h.s. of Eq. (4.4) represents the complex conjugation, which is used to invert the direction of the plane wave. A cubic group analysis shows that the two-nucleon source Eq. (4.4) contains the orbital contribution $A_1^+ \oplus E^+ \oplus T_1^-$, whose main components are S-wave, D-wave and P-wave, respectively. Thus the two-nucleon source Eq. (4.4) covers all the two-nucleon channels with $J \leq 2$.

For the spin-triplet odd-parity sector, Eq. (4.4) generates the lowest-lying NBS wave functions for $(J^P, I) = (A_1^-, 1), (T_1^-, 1), (E^-, 1)$ and $(T_2^-, 1)$, which roughly correspond to $J^P = 0^-, 1^-, 2^-$ and 2^- , respectively. Among these, we consider Schrödinger equations for three NBS wave functions in $J^P = A_1^-, T_1^-, T_2^-$ as

$$\left[H_0 + V_C(r) + V_T(r)S_{12} + V_{LS}(r)\mathbf{L} \cdot \mathbf{S} \right] \varphi^W(\mathbf{r}; J^P) = E_0(J^P) \varphi^W(\mathbf{r}; J^P), \quad (4.6)$$

where $E_0(J^P) = k^2/m_N$ from the lowest-lying energy $W = 2\sqrt{m_N^2 + k^2}$ for the J^P sector. In order to obtain $V_C(r)$, $V_T(r)$ and $V_{LS}(r)$ in odd parity sectors, Eqs. (4.6) for $J^P = A_1^-, T_1^-, T_2^-$, which correspond to 3P_0 , 3P_1 and ${}^3P_2 + {}^3F_2$, are solved.

Numerical calculations are performed by using 2 flavor QCD gauge configurations on $16^3 \times 32$ lattice generated by CP-PACS Collaboration,^{39),40)} with Iwasaki gauge action at $\beta = 1.95$ and $O(a)$ improved Wilson (clover) quark action at $\kappa = 0.1375$. This setup leads to the lattice spacing $a^{-1} = 1.27$ GeV ($a \simeq 1.555$ fm), the pion mass $m_\pi \simeq 1136$ MeV, the nucleon mass $m_N \simeq 2165$ MeV. The spatial extension amounts to $L = 16a \simeq 2.5$ fm.

Fig. 9 shows preliminary results of the central potential $V_C(r)$, tensor potential $V_T(r)$ and the spin-orbit force $V_{LS}(r)$ in the spin-triplet odd parity sector. They have the following qualitative features. (1) $V_C(r)$ has repulsive core at short distance. (2) $V_T(r)$ is positive and very small. (3) $V_{LS}(r)$ is large and negative at short distance. These features qualitatively agree with those of phenomenological potentials.⁸⁾

§5. Hyperon Interactions

Study of hyperon-nucleon (YN) and hyperon-hyperon (YY) interactions is one of the challenges in contemporary nuclear physics. These potentials give a key to

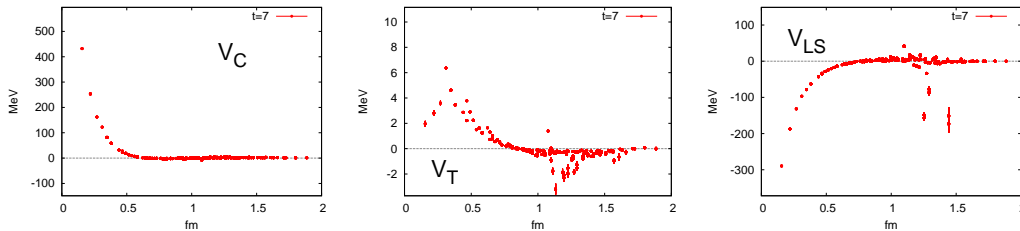


Fig. 9. Potentials in odd parity sector obtained from 3P_0 , 3P_1 and ${}^3P_2 + {}^3F_2$ NBS wave functions calculated at $m_\pi = 1136$ MeV. Left, middle, and right figures show central, tensor and spin-orbit force in parity odd sector, respectively.

understand nuclear many-body systems with strangeness. Also they are essential to explore the structure of the neutron star core, where strangeness degree of freedom is expected to appear. At present, experimental data on YN and YY scatterings are not sufficient to make precise constraints on the hyperon potentials, while spectroscopic studies of Λ hypernuclei, performed by employing various reactions such as (π^+, K^+) , (K^-, π^-) and $(e, e'K^+)$,^{41), 42)} give some information on the ΛN interactions. Under these circumstances, studies on the basis of lattice QCD is quite important as an alternative method to access YN and YY interactions. In this section we mainly consider potentials in the strangeness $S = -1$ sector, obtained from $2 + 1$ flavor lattice QCD simulations with PACS-CS gauge configurations. A study on potentials between octet baryons in the flavor $SU(3)$ limit and coupled channel analysis on potentials in the strangeness $S = -2$ sector beyond the $SU(3)$ limit will be discussed in the next two sections.

5.1. ΛN and ΣN potentials in full QCD

The ΛN and the ΣN ($I = 3/2$) are the lowest states in the strangeness $S = -1$ systems with $I = 1/2$ and $I = 3/2$, respectively. Therefore potentials for these states can be calculated as in the case of NN potential. In Ref. 43), the ΛN potential and the ΣN potential with $I = 3/2$ are calculated by using $2+1$ flavor full QCD gauge configurations with the original time-independent HAL QCD method. In the following, we show improved results on a $32^3 \times 64$ lattice at $a = 0.091(1)$ fm with the time-dependent HAL QCD method discussed in Sec. 3.4.

The ΛN (left panel) and the $\Sigma N(I = 3/2)$ (right panel) potentials in the 1S_0 channel are shown in Fig. 10. In the $2+1$ flavor QCD, while the ΣN ($I = 3/2$) potential still belongs directly to the $\mathbf{27}(I = 3/2)$ representation thanks to the isospin symmetry, an energy eigenstate of a ΛN system in the 1S_0 channel is a mixture of $\mathbf{27}(I = 1/2)$ and $\mathbf{8}_s$ in the flavor representation, so that these two potentials are not necessarily equal. In the present $2 + 1$ flavor QCD calculation shown in Fig. 10, these potentials look similar due to small flavor- $SU(3)$ breaking: For example, our hadron masses are $(m_\pi, m_K, m_N, m_\Lambda, m_\Sigma) = (0.7006(4), 0.7879(4), 1.574(3), 1.635(3), 1.650(3))$ GeV. The left panel of Fig. 11 shows the central potential (circle) and the tensor potential (triangle) of the ΛN system in the ${}^3S_1 - {}^3D_1$ channel, whose eigenstate is a mixture of $\overline{\mathbf{10}}$ and $\mathbf{8}_a$. The attractive well at distance $r \approx 0.6$ fm is deeper than that of the

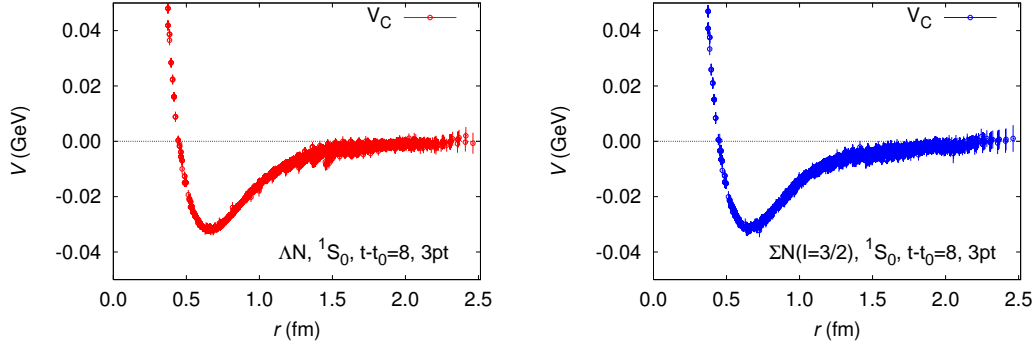


Fig. 10. Left: The central potential in the 1S_0 channel of the ΛN system in 2 + 1 flavor QCD as a function of r . Right: The central potential in the 1S_0 channel of the $\Sigma N(I = 3/2)$ system as a function of r .

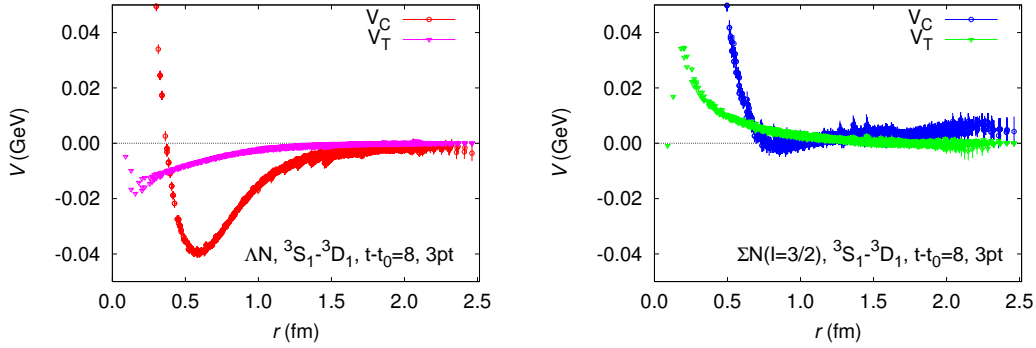


Fig. 11. Left: The central potential (circle) and the tensor potential (triangle) in the $^3S_1 - ^3D_1$ channel of the ΛN system as a function of r . Right: The central potential (circle) and the tensor potential (triangle) in the $^3S_1 - ^3D_1$ channel of the $\Sigma N(I = 3/2)$ system as a function of r .

ΛN central potential in the 1S_0 channel, while the tensor potential itself (triangle) is weaker than the tensor potential in the NN system.⁴⁴⁾

The right panel of Fig. 11 shows the central potential (circle) and the tensor potential (triangle) of the $\Sigma N(I = 3/2)$ system in the $^3S_1 - ^3D_1$ channel. Due to the isospin symmetry, this channel belongs solely to the flavor $\mathbf{10}$ representation without mixture of $\overline{\mathbf{10}}$ or $\mathbf{8}_a$. As seen from the figure, there is no clear attractive well in the central potential (circle). This repulsive nature of the $\Sigma N(I = 3/2, ^3S_1 - ^3D_1)$ central potential is consistent with the prediction from the naive quark model.⁴⁵⁾ The tensor force is a little stronger than that of the ΛN system but is still weaker in magnitude than that of the NN system.

5.2. ΞN potential in quenched QCD

Experimentally, not much information is available on the $N\Xi$ interaction except for a few studies: a recent report gives the upper limit of elastic and inelastic cross sections⁴⁶⁾ while earlier publications suggest weak attractions of Ξ -nuclear interactions.^{47)–49)} The Ξ -nucleus interactions will be soon studied as one of the

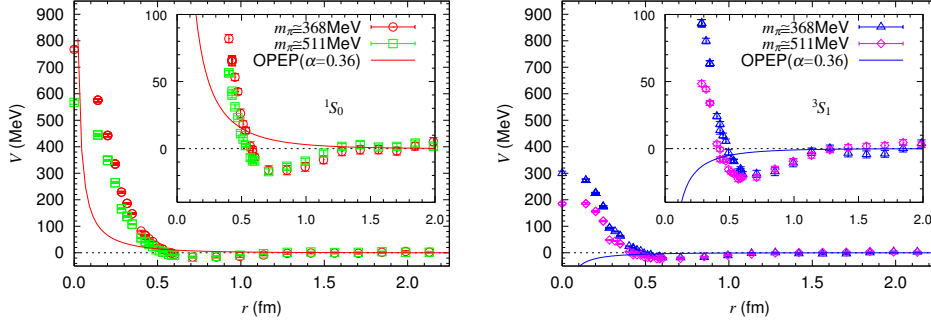


Fig. 12. (Left) The spin-singlet central potential for $p\Xi^0$ obtained from the orbital A_1^+ channel at $m_\pi \simeq 368$ MeV (circle) and $m_\pi \simeq 511$ MeV (box). The central part of the OPEP ($F/(F+D) = 0.36$) in Eq. (5-2) is also given by solid line. (Right) The spin-triplet effective central potential from the orbital A_1^+ channel at $m_\pi \simeq 368$ MeV (triangle) and $m_\pi \simeq 511$ MeV (diamond), together with the OPEP (solid line). Taken from Ref. 51).

day-one experiments at J-PARC⁵⁰⁾ via (K^-, K^+) reaction with a nuclear target. Ref. 51) gives the first result of the potential in $I = 1$ $N\Xi$ system, which does not show strong decay into other channels. Lattice parameters are the same as for the quenched NN potential in Sec.4.1, but the method to determine the lattice spacing in Ref. 51) is a little different from the one in Sec.4.1. The potential is calculated at $(m_\pi, m_N, m_\Xi) = (511(1) \text{ MeV}, 1300(4) \text{ MeV}, 1419(4) \text{ MeV})$ and $(368(1) \text{ MeV}, 1167(7) \text{ MeV}, 1383(6) \text{ MeV})$ with the interpolation operators

$$p_\alpha(x) = \varepsilon_{abc}(u_a^T(x)C\gamma_5 d_b(x))u_{c,\alpha}(x), \quad \Xi_\alpha^0(x) = \varepsilon_{abc}(u_a^T(x)C\gamma_5 s_b(x))s_{c,\alpha}(x). \quad (5.1)$$

Since both p and Ξ^0 have $(I, I_z) = (1/2, 1/2)$, the $p\Xi^0$ system has $I = 1$ with the strangeness $S = -2$.

The left (right) of Fig. 12 gives the (effective) central potential of the $p\Xi^0$ system obtained from the $L = A_1^+$ representation for the spin-singlet (triplet) at $m_\pi = 511$ MeV and 368 MeV. Potentials in the $I = 1$ $N\Xi$ system for both channels show a repulsive core at $r \leq 0.5$ fm surrounded by an attractive well, similar to the NN systems. In contrast to the NN case, however, the repulsive core of the $p\Xi^0$ potential in the spin-singlet channel is substantially stronger than in the triplet channel. The attraction in the medium to long distance region ($0.6 \text{ fm} \leq r \leq 1.2 \text{ fm}$) is similar in both channels. The height of the repulsive core increases as the light quark mass decreases, while a significant difference is not seen for the attraction in the medium to long distance within statistical errors. Potentials in Fig. 12 are weakly attractive on the whole in both spin channels at both pion masses, in spite of the repulsive core at short distance, and the attraction in the triplet is a little stronger than that in the singlet.

The solid lines in Fig. 12 are the one-pion exchange potential (OPEP), given by

$$V_C^\pi = -(1 - 2\alpha) \frac{g_{\pi NN}^2}{4\pi} \frac{(\boldsymbol{\tau}_N \cdot \boldsymbol{\tau}_\Xi)(\boldsymbol{\sigma}_N \cdot \boldsymbol{\sigma}_\Xi)}{3} \left(\frac{m_\pi}{2m_N} \right)^2 \frac{e^{-m_\pi r}}{r} \quad (5.2)$$

with $(m_\pi, m_N) = (368 \text{ MeV}, 1167 \text{ MeV})$, where the pseudo-vector $\pi\Xi\Xi$ coupling $f_{\pi\Xi\Xi}$

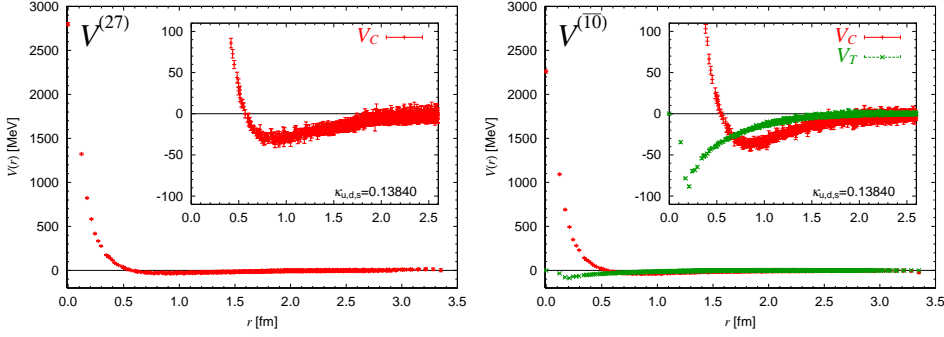


Fig. 13. The BB potentials in $\mathbf{27}$ (Left) and $\overline{\mathbf{10}}$ (Right) representations extracted from the lattice QCD simulation at $M_{\text{ps}} = 469$ MeV. Taken from Ref. 56).

is related to the πNN coupling as $f_{\pi\Xi\Xi} = -f_{\pi NN}(1 - 2\alpha)$ with the parameter $\alpha = F/(F + D)$, and $g_{\pi NN} = f_{\pi NN} \frac{m_\pi}{2m_N}$. The empirical values, $\alpha \simeq 0.36$ and $g_{\pi NN}/(4\pi) \simeq 14.0$, are used for the plot. Unlike the NN potential, the OPEP in the present case has opposite sign between the spin-singlet channel and spin-triplet channel. In addition, the absolute magnitude is smaller due to the factor $1 - 2\alpha$. No clear signature of the OPEP at long distance ($r \geq 1.2$ fm) is yet observed in Fig. 12 within statistical errors.

§6. Baryon interaction in the flavor SU(3) limit

6.1. Potentials in the flavor SU(3) limit

In order to reveal the nature of the hyperon interactions in various channels, it is more convenient to consider an idealized flavor SU(3) symmetric world, where u, d and s quarks are all degenerate with a common finite mass. In this limit, one can capture essential features of the interaction, in particular, the short range force without contamination from the quark mass difference.

In the flavor SU(3) limit, the ground state baryon belongs to the flavor-octet with spin 1/2, and two-baryon states with a given angular momentum can be labeled by the irreducible representation of SU(3) as

$$\mathbf{8} \otimes \mathbf{8} = \underbrace{\mathbf{27} \oplus \mathbf{8} \oplus \mathbf{1}}_{\text{symmetric}} \oplus \underbrace{\overline{\mathbf{10}} \oplus \mathbf{10} \oplus \mathbf{8}}_{\text{anti-symmetric}}, \quad (6-1)$$

where "symmetric" and "anti-symmetric" stand for the symmetry under the exchange of the flavor for two baryons. For the system with orbital S-wave, the Pauli principle for baryons imposes $\mathbf{27}$, $\mathbf{8}$ and $\mathbf{1}$ to be spin-singlet (1S_0), while $\overline{\mathbf{10}}$, $\mathbf{10}$ and $\mathbf{8}$ to be spin-triplet ($^3S_1 - ^3D_1$). Calculations in the SU(3) limit allow us to extract potentials for these six flavor irreducible multiplets as follows.

A two-baryon operator $BB^{(X)}$ which belongs to one definite flavor representation X , can be given in terms of the baryon base operator with the corresponding Clebsch-Gordan (CG) coefficients C_{ij}^X as $BB^{(X)} = \sum_{ij} C_{ij}^X B_i B_j$. By using this operator at source and/or sink, the NBS wave function for two-baryon system in the flavor

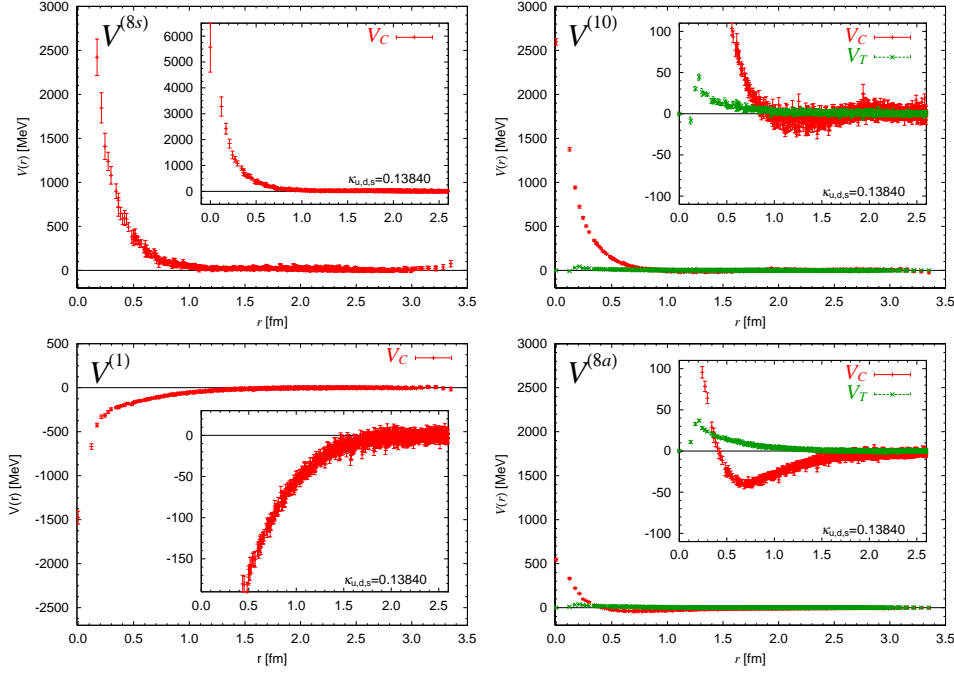


Fig. 14. The BB potentials in $\mathbf{8}_s$ (Upper-Left), $\mathbf{10}$ (Upper-Right), $\mathbf{1}$ (Lower-Left) and $\mathbf{8}_a$ (Lower-Right) extracted from the lattice QCD simulation at $M_{ps} = 469$ MeV. Taken from Ref. 56).

representation can be obtained. Potentials in the flavor base, $V^{(X)}(r)$, are extracted from such wave functions in the same manner for nuclear forces explained in Sec. 3.

In Ref.52), the (effective) central potentials are calculated in the original time-independent HAL QCD method by using the 3 flavor full QCD gauge configuration⁵³⁾ on a $16^3 \times 32$ lattice at $a \simeq 0.12$ fm, and at two values of quark hopping parameter corresponding to $(M_{ps}, M_B) = (1014(1)\text{MeV}, 2026(3)\text{MeV})$ and $(835(1)\text{ MeV}, 1752(3)\text{ MeV})$, where M_{ps} and M_B denote the octet pseudo-scalar (PS) meson mass and the octet baryon mass, respectively. In Refs. 54)–56), on the other hand, the central and tensor potentials are calculated in the time-dependent HAL QCD method discussed in Sec.3.4 by using the 3 flavor full QCD gauge configuration generated by HAL QCD Collaboration on a $32^3 \times 32$ lattice at $a \simeq 0.12$ fm, and at five values of quark hopping parameter which correspond to $(M_{ps}, M_B) = (1170.9(7)\text{MeV}, 2274(2)\text{MeV})$, $(1015(1)\text{ MeV}, 2030(2)\text{ MeV})$, $(837(1)\text{ MeV}, 1748(1)\text{ MeV})$, $(673(1)\text{ MeV}, 1485(2)\text{ MeV})$, and $(468.6(7)\text{ MeV}, 1161(2)\text{ MeV})$. Figs. 13 and 14 show the flavor basis potentials for $M_{ps} = 469$ MeV.⁵⁶⁾ The left panels show central potentials for the spin-singlet channel from the $J^P = A_1^+$ state, while the right panels give central (V_C) and tensor (V_T) potentials for the spin-triplet channel from the $J^P = T_1^+$ state.

As listed in Table III, some of octet-baryon pairs solely belong to an irreducible representation of flavor SU(3). For example, symmetric NN belongs to $\mathbf{27}$ representation. Therefore, $V^{(\mathbf{27})}(r)$ can be considered as flavor SU(3) symmetric limit of the NN spin-singlet (1S_0) potential. Similarly $V^{(\mathbf{10})}$, $V^{(\mathbf{10})}$ and $V^{(\mathbf{8}_a)}$ can be considered as flavor SU(3) symmetric limit of some BB potentials of the particle basis, while

flavor multiplet	baryon pair (isospin)
27	$\{NN\}(I=1), \{N\Sigma\}(I=3/2), \{\Sigma\Sigma\}(I=2),$ $\{\Sigma\varepsilon\}(I=3/2), \{\varepsilon\varepsilon\}(I=1)$
8_s	none
1	none
10*	$[NN](I=0), [\Sigma\varepsilon](I=3/2)$
10	$[N\Sigma](I=3/2), [\varepsilon\varepsilon](I=0)$
8_a	$[N\varepsilon](I=0)$

Table III. Baryon pairs which belongs to an irreducible flavor SU(3) representation, where $\{BB'\}$ and $[BB']$ denotes $BB' + B'B$ and $BB' - B'B$, respectively.

$V^{(1)}$ and $V^{(8_s)}$ are always mixtures of different BB potentials in the particle basis.

Fig. 13 shows $V_C^{(27)}(r)$ and $V_{C,T}^{(\overline{10})}(r)$, which correspond to spin-singlet and spin-triplet NN potentials, respectively. Both central potentials have a repulsive core at short distance with an attractive pocket around 0.8 fm. These qualitative features are consistent with the results found for the NN potential in previous section. The upper-right panel of Fig. 14 shows that $V_C^{(10)}(r)$ has a stronger repulsive core and a weaker attractive pocket compared to $V_C^{(27)}(r)$ and $V_C^{(\overline{10})}(r)$. Furthermore $V_C^{(8_s)}(r)$ in the upper-left panel of Fig. 14 has a very strong repulsive core among all 6 channels, while $V_C^{(8_a)}(r)$ in the lower-right panel has a very weak repulsive core. In contrast to all other cases, $V_C^{(1)}(r)$ has attraction at short distances instead of repulsion, as shown in the lower-left panel.

Above features are consistent with what has been observed in a SU(6) quark model.⁴⁵⁾ In particular, the potential in the 8_s channel in this quark model becomes strongly repulsive at short distance since the six quarks cannot occupy the same orbital state due to the Pauli exclusion for quarks. On the other hand, the potential in the 1 channel does not suffer from the quark Pauli exclusion at all, and can become attractive due to the short-range gluon exchange. Such agreements between the lattice data and the quark model suggest that the quark Pauli exclusion plays an essential role for the repulsive core in BB systems.

The potential for the flavor singlet is entirely attractive even at very short distance. This might produce a bound state, the H -dibaryon, in this channel. We will discuss this possibility in the next subsection.

In the flavor SU(3) limit, the BB potentials in the particle basis can be obtained from those in flavor basis by a unitary rotation as

$$V_{ij}(r) = \sum_X U_{iX} V^{(X)}(r) U_{Xj}^* \quad (6.2)$$

where U_{iX} is a unitary matrix which rotates the flavor basis $|X\rangle$ to the particle basis $|i\rangle$ as $|i\rangle = U_{iX}|X\rangle$, and given in terms of the CG coefficients. The explicit forms of the unitary matrix U are found in Ref. 52).

In Fig. 15, we show BB potentials for S=-2, I=0, 1S_0 sector at $M_{PS} = 469$ MeV, as a characteristic example. The flavor base potentials are fitted by the analytic function composed of an attractive Gaussian core plus a long range (Yukawa)²

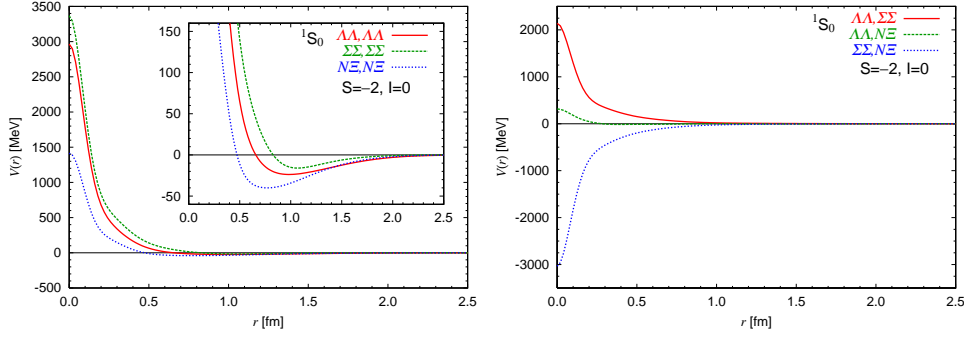


Fig. 15. BB potentials in particle basis for the $S=-2$, $I=0$, 1S_0 sector. Three diagonal(off-diagonal) potentials are shown in left(right) panel.

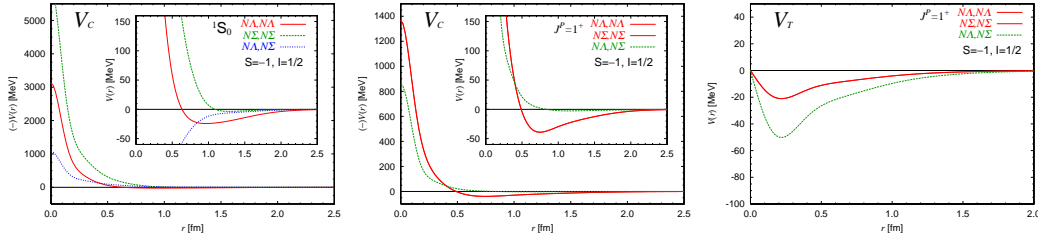


Fig. 16. BB potentials in particle basis for the $S=-1$, $I=1/2$ sector, 1S_0 (Left), spin-triplet V_C (Center) and spin-triplet V_T (Right), extracted from the lattice QCD simulation at $M_{ps} = 469$ MeV.

attraction,

$$V(r) = b_1 e^{-b_2 r^2} + b_3 (1 - e^{-b_4 r^2})^2 \left(\frac{e^{-b_5 r}}{r} \right)^2, \quad (6.3)$$

with five parameters $b_{1,2,3,4,5}$. The left panel of Fig. 15 shows the diagonal potentials. One observes that all three diagonal potentials have a repulsive core. The repulsion is most strong in the $\Sigma\Sigma(I=0)$ channel, reflecting its largest CG coefficient of the $\mathbf{8}_s$ state among three channels, while the attraction in the $\mathbf{1}$ state is reflected most in the $N\Sigma(I=0)$ potential due to its largest CG coefficient. The right panel of Fig. 15 shows the off-diagonal potentials, which are comparable in magnitude to the diagonal ones, except for the $\Lambda\Lambda-N\Sigma$ transition potential. Since the off-diagonal parts are not negligible in the particle basis, a fully coupled channel analysis is necessary to study observables in this system. This is important when we study the real world with the flavor $SU(3)$ breaking, where only the particle base is meaningful.

As another example, we show BB potentials for $S=-1$, $I=1/2$ sector at $M_{ps} = 469$ MeV in Fig. 16. The left panel of Fig. 16 shows the potential in the 1S_0 channel, while the center (right) panel of Fig. 16 shows the central (tensor) potential for $J^P = T_1^+$ spin-triplet channel. We observe that the off-diagonal $N\Lambda-N\Sigma$ potentials are significantly large, especially in the spin-triplet channel, so that the full $N\Lambda-N\Sigma$ coupled channel analysis is also necessary to study observables. In addition, the repulsive cores in the spin-single channel are much stronger than that in the spin-

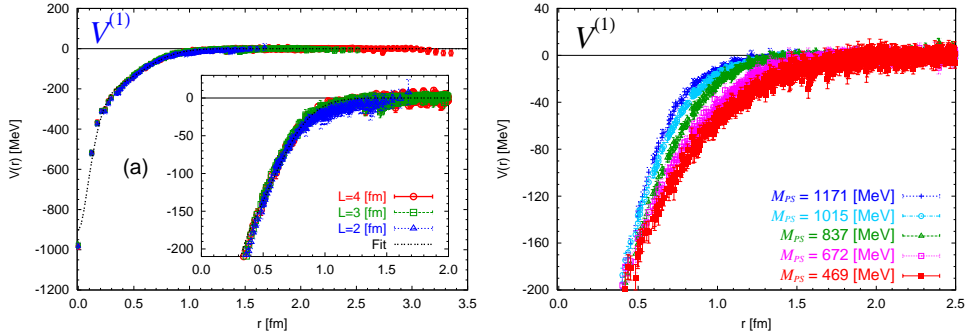


Fig. 17. The flavor-singlet potential $V_C^{(1)}(r)$ at $(t - t_0)/a = 10$. (Left) Results for $L = 1.94, 2.90, 3.87$ fm at $M_{ps} = 1015$ MeV. (Right) Results for $L = 3.87$ fm at $M_{ps} = 1171, 1015, 837, 672, 469$ MeV.

triplet channel, due to the strong repulsion of the $\mathbf{8}_s$ state, which couples only to the spin-singlet channel.

Although all quark masses of 3 flavors are degenerate and rather heavy in the present simulations, these particle base potentials, shown in Fig. 15 and Fig. 16, may provide useful information for the behavior of hyperons in hyper-nuclei and in neutron stars.^{42), 57)} BB potentials in all other sectors can be found in Ref. 52).

6.2. Bound H dibaryon in the flavor $SU(3)$ limit

In this subsection, we investigate the potential of the flavor singlet channel in order to see whether the bound H dibaryon exists or not in the flavor $SU(3)$ limit case.

Potentials for the flavor irreducible channels in the $SU(3)$ limit have been calculated in Ref. 54)–56) on $16^3 \times 32$, $24^3 \times 32$ and $32^3 \times 32$ lattices at $a = 0.121(2)$ fm and five values of the quark mass, as mentioned before.

Shown in Fig. 17(Left) and Fig. 17(Right) are the volume and the quark mass dependencies of the central potential in the flavor-singlet channel $V_C^{(1)}(r)$ at $(t - t_0)/a = 10$, where the potentials do not have appreciable change with respect to the choice of t . The flavor-singlet potential is shown to have an “attractive core” and to be well localized in space. Because of the latter property, no significant volume dependence of the potential is observed within the statistical errors, as seen in Fig. 17(Left). As the quark mass decreases in Fig. 17(Right), the long range part of the attraction tends to increase.

The resultant potential is fitted by the form in Eq. (6.3). With the five parameters, $b_{1,2,3,4,5}$, the lattice results can be fitted reasonably well with $\chi^2/\text{dof} \simeq 1$. The fitted result for $L = 3.87$ fm is shown by the dashed line in Fig. 17(Left).

Solving the Schrödinger equation with the fitted potential in infinite volume, the energies and the wave functions are obtained at the present quark masses in the flavor $SU(3)$ limit. It turns out that, at each quark mass, there is only one bound state with binding energy of 20–50 MeV. Fig. 18(Left) shows the energy and the root-mean-squared (rms) distance of the bound state at each quark mass obtained from the potential at $L = 3.87$ fm and $(t - t_0)/a = 10$, where errors are estimated by

the jackknife method. Despite the fact that the potential becomes more attractive as quark mass decrease, the resultant binding energies of the H -dibaryon decrease in the present range of the quark masses, since the increase of the attraction toward the lighter quark mass is compensated by the increase of the kinetic energy for the lighter baryon mass. It is noted that there appears no bound state for the potential of the 27-plet channel or the $\overline{10}$ -plet channel ("deuteron") in the present range of the quark masses.

By including systematic errors caused by the choice of sink-time t in $R(\mathbf{r}, t - t_0)$, the final results of the binding energy B_H and the rms distance $\sqrt{\langle r^2 \rangle}$ are summarized below, where the 1st and 2nd parentheses correspond to statistical and systematic errors, respectively.

$$\begin{aligned}
 M_{\text{ps}} = 1171 \text{ MeV} : & \quad B_H = 49.1(3.4)(5.5) \text{ MeV} \quad \sqrt{\langle r^2 \rangle} = 0.685(13)(25) \text{ fm} \\
 M_{\text{ps}} = 1015 \text{ MeV} : & \quad B_H = 37.2(3.7)(2.4) \text{ MeV} \quad \sqrt{\langle r^2 \rangle} = 0.809(23)(10) \text{ fm} \\
 M_{\text{ps}} = 837 \text{ MeV} : & \quad B_H = 37.8(3.1)(4.2) \text{ MeV} \quad \sqrt{\langle r^2 \rangle} = 0.865(20)(25) \text{ fm} \\
 M_{\text{ps}} = 672 \text{ MeV} : & \quad B_H = 33.6(4.8)(3.5) \text{ MeV} \quad \sqrt{\langle r^2 \rangle} = 1.029(41)(23) \text{ fm} \\
 M_{\text{ps}} = 469 \text{ MeV} : & \quad B_H = 26.0(4.4)(4.8) \text{ MeV} \quad \sqrt{\langle r^2 \rangle} = 1.247(70)(59) \text{ fm}.
 \end{aligned}$$

Recently, the existence of H -dibaryon is also investigated by a direct calculation of its binding energy in 2+1 full QCD simulations,^{58),59)} where $B_H = 13.2(1.8)(4.0)$ MeV is reported in the $L \rightarrow \infty$ extrapolation at $m_\pi \simeq 389$ MeV, $m_K \simeq 544$ MeV. Fig. 18(Right) gives a summary of the H -dibaryon binding energy from full QCD simulations recently reported.

Since the binding energy is comparable to the splitting between physical hyperon masses and not so sensitive to quark mass, there may be a possibility of weakly bound or resonant H -dibaryon even in the real world with lighter quark masses and the flavor SU(3) breaking. Our phenomenological trial analysis using 3-flavor lattice QCD results, suggests a resonant H -dibaryon above $\Lambda\Lambda$ but bellow $N\Sigma$ thresholds.⁵⁶⁾ To make a definite conclusion on this point, however, the $\Lambda\Lambda - N\Sigma - \Sigma\Sigma$ coupled channel analysis is necessary for H in the (2+1)-flavor lattice QCD simulations, as will be discussed in Sec. 7.

§7. Hadronic interactions above inelastic threshold

In this section, we discuss a method to investigate hadron interactions above inelastic threshold by generalizing the HAL QCD method. Then, we apply the method to coupled channel potentials in the $S = -2$ and $I = 0$ sector.

7.1. Coupled-channel approach to inelastic scattering

For simplicity, let us discuss a case of $A+B \rightarrow C+D$ scattering where A, B, C, D represent some 1-particle states. This is a simplified version of the octet baryon scattering in the strangeness $S = -2$ and isospin $I = 0$ channel, where $\Lambda\Lambda$, $N\Sigma$ and $\Sigma\Sigma$ appear as asymptotic states of the strong interaction if the total energy is larger than $2m_\Sigma$. We here assume $m_A + m_B < m_C + m_D < W$, where $W = E_k^A + E_k^B$

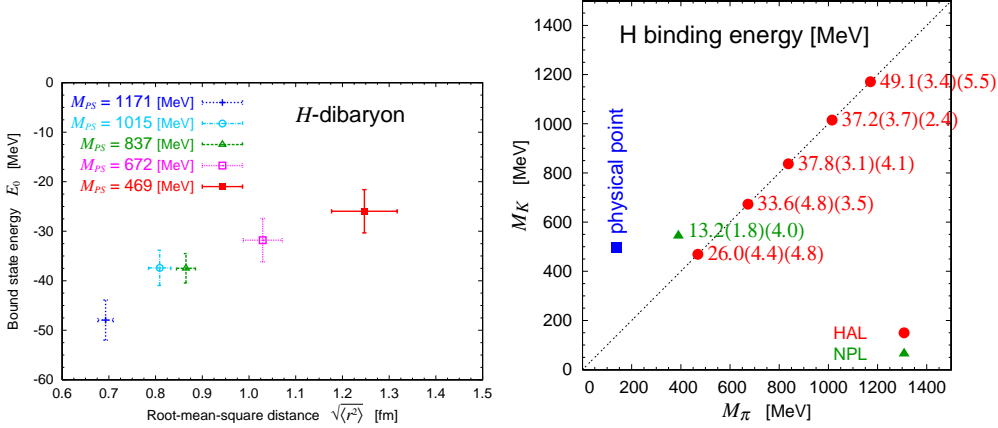


Fig. 18. (Left) The energy E_0 and the root-mean-square distance $\sqrt{\langle r^2 \rangle}$ of the bound state in the flavor singlet channel at each quark mass. Bars represent statistical errors only. (Right) Summary of the H -dibaryon binding energy in recent full QCD simulations. HAL stands for the present results and NPL stands for the result in Ref.⁵⁹⁾

is the total energy of the system, and $E_k^X = \sqrt{m_X^2 + \mathbf{k}^2}$. In this case, the QCD eigenstate with the quantum numbers of the AB state and center of mass energy W is expressed as

$$|W\rangle = c_{AB}|AB, W\rangle + c_{CD}|CD, W\rangle + \dots \quad (7.1)$$

$$|AB, W\rangle = |A, \mathbf{k}\rangle_{\text{in}} \otimes |B, -\mathbf{k}\rangle_{\text{in}}, \quad |CD, W\rangle = |C, \mathbf{q}\rangle_{\text{in}} \otimes |D, -\mathbf{q}\rangle_{\text{in}}, \quad (7.2)$$

where $W = E_k^A + E_k^B = E_q^C + E_q^D$. Then we define the following NBS wave functions,

$$\varphi_{AB}(\mathbf{r}, \mathbf{k})e^{-Wt} = \langle 0|T\{\varphi_A(\mathbf{x} + \mathbf{r}, t)\varphi_B(\mathbf{x}, t)\}|W\rangle, \quad (7.3)$$

$$\varphi_{CD}(\mathbf{r}, \mathbf{q})e^{-Wt} = \langle 0|T\{\varphi_C(\mathbf{x} + \mathbf{r}, t)\varphi_D(\mathbf{x}, t)\}|W\rangle. \quad (7.4)$$

Using the partial wave decomposition such that^{*)}

$$\varphi_X(\mathbf{r}, \mathbf{k}) = 4\pi \sum_{l,m} i^l \varphi_X^l(r, k) Y_{lm}(\Omega_{\mathbf{r}}) \overline{Y_{lm}(\Omega_{\mathbf{k}})} \quad (7.5)$$

for $X = AB$ or CD , it can be shown⁶¹⁾ that these wave functions satisfy

$$(\nabla^2 + \mathbf{k}^2)\varphi_{AB}(\mathbf{r}, \mathbf{k}) = 0, \quad (\nabla^2 + \mathbf{q}^2)\varphi_{CD}(\mathbf{r}, \mathbf{q}) = 0 \quad (7.6)$$

for $r \rightarrow \infty$.

Let us now consider QCD in the finite volume V where $|AB, W\rangle$ and $|CD, W\rangle$ are no longer eigenstates of the Hamiltonian. True eigenvalues are shifted from W to $W_i = W + O(V^{-1})$ ($i = 1, 2$). By the diagonalization method in lattice QCD, it is relatively easy to determine W_1 and W_2 . With these values Lüscher's finite volume formula gives two conditions, which, however, are insufficient to determine

^{*)} Here we ignore spins for simplicity.

three observables, two scattering phase shifts δ_ℓ^1 , δ_ℓ^2 and one mixing angle θ . We here explain a new approach proposed in Refs.(60), (61) to overcome this difficulty. Let us consider the NBS wave functions at two different values of energy, W_1 and W_2 , in the finite volume:

$$\varphi_X(\mathbf{x}, \mathbf{p}_i^X) e^{-W_i t} = \langle 0 | T \{ \varphi_{X_1}(\mathbf{x} + \mathbf{r}, t) \varphi_{X_2}(\mathbf{r}, t) \} | W_i \rangle, \quad i = 1, 2. \quad (7.7)$$

where $X (= X_1 X_2) = AB$ or CD with $\mathbf{p}^{AB} = \mathbf{k}$ or $\mathbf{p}^{CD} = \mathbf{q}$. We then define the coupled channel non-local potentials from the coupled channel Schrödinger equation as

$$\left[\frac{(\mathbf{p}_i^X)^2}{2\mu_X} - H_0 \right] \varphi_X(\mathbf{x}, \mathbf{p}_i^X) = \sum_Y \int d^3y U_{X,Y}(\mathbf{x}, \mathbf{y}) \varphi_Y(\mathbf{y}, \mathbf{p}_i^Y) \quad (7.8)$$

for $i = 1, 2$ where the reduced mass is defined by $1/\mu_X = 1/m_{X_1} + 1/m_{X_2}$. In the leading order of the velocity expansion, we have

$$K_X(\mathbf{x}, \mathbf{p}_i^X) \equiv \left[\frac{(\mathbf{p}_i^X)^2}{2\mu_X} - H_0 \right] \varphi_X(\mathbf{x}, \mathbf{p}_i^X) = \sum_Y V_{X,Y}(\mathbf{x}) \varphi_Y(\mathbf{x}, \mathbf{p}_i^Y) \quad (7.9)$$

These equations for $i = 1, 2$ can be solved as

$$\begin{pmatrix} V_{AB,AB}(\mathbf{x}) & V_{AB,CD}(\mathbf{x}) \\ V_{CD,AB}(\mathbf{x}) & V_{CD,CD}(\mathbf{x}) \end{pmatrix} = \begin{pmatrix} K_{AB}(\mathbf{x}, \mathbf{k}_1) & K_{AB}(\mathbf{x}, \mathbf{k}_2) \\ K_{CD}(\mathbf{x}, \mathbf{q}_1) & K_{CD}(\mathbf{x}, \mathbf{q}_2) \end{pmatrix} \times \begin{pmatrix} \varphi_{AB}(\mathbf{x}, \mathbf{k}_1) & \varphi_{AB}(\mathbf{x}, \mathbf{k}_2) \\ \varphi_{CD}(\mathbf{x}, \mathbf{q}_1) & \varphi_{CD}(\mathbf{x}, \mathbf{q}_2) \end{pmatrix}^{-1}. \quad (7.10)$$

Once we obtain the coupled channel local potentials $V_{X,Y}(\mathbf{x})$, we solve the coupled channel Schrödinger equation in *infinite* volume with some appropriate boundary condition such that the incoming wave has a definite ℓ and consists of the AB state only, in order to extract three observables for each ℓ ($\delta_\ell^1(W)$, $\delta_\ell^2(W)$ and $\theta_\ell(W)$) at all values of W . Of course, since $V_{X,Y}$ is the leading order approximation in the velocity expansion of $U_{X,Y}(\mathbf{x}, \mathbf{y})$, results for three observables $\delta_\ell^1(W)$, $\delta_\ell^2(W)$ and $\theta(W)$ at $W \neq W_1, W_2$ are also approximate ones and might be different from the exact values. By performing an additional extraction of $V_{X,Y}(\mathbf{x})$ at $(W_3, W_4) \neq (W_1, W_2)$, we can test how good the leading order approximation is.

The method considered above can be generalized to inelastic scattering where a number of particles is not conserved such that $A+B \rightarrow A+B$ and $A+B \rightarrow A+B+C$. See Ref. (61) for more details.

7.2. Coupled-channel potentials in $(S, I) = (-2, 0)$ channel

As an application of the method in the previous subsection, let us consider BB potentials for the $S = -2$ and $I = 0$ system, i.e., the coupled $\Lambda\Lambda-N\Sigma-\Sigma\Sigma$ system. It is interesting to investigate this system since it involves the flavor single state, which is free from the Pauli blocking of quark degrees of freedom at short distance. Since mass differences of these BB systems are quite small, all 3 states appear in

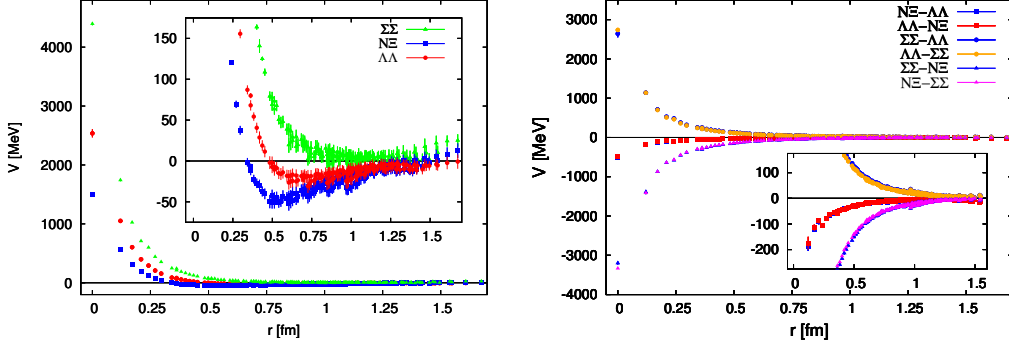


Fig. 19. The coupled channel potential matrix from the NBS wave function for Set 1. The vertical axis is the potential strength in units of MeV, while the horizontal axis is the relative distance between two baryons in units of fm.

NBS wave functions. The coupled channel method in the previous subsection can be applied to treat such complicated systems.

At the leading order of the velocity expansion, the coupled channel 3×3 potential matrix in this case is given by

$$V_{X,Y}(\mathbf{x}) = \sum_{i=1}^3 K_X^i(\mathbf{x}, \mathbf{p}_i^X) \left[\varphi_Y^{W_i}(\mathbf{x}, \mathbf{p}_i^Y) \right]^{-1}, \quad (7.11)$$

where i is a label for energy W_i and $X, Y = \Lambda\Lambda, N\Xi$ or $\Sigma\Sigma$. Here the last factor is the inverse of the 3×3 matrix $\varphi_A^{W_i}(\mathbf{r}, \mathbf{k}_A^i)$ with indices i and A .

Gauge configurations generated by CP-PACS/JLQCD Collaborations on a $16^3 \times 32$ lattice at $a \simeq 0.12$ fm (therefore $L \simeq 1.9$ fm) in 2+1-flavor full QCD simulations are employed to calculate the coupled channel potentials at three different values of the light quark mass with the fixed bare strange quark mass.⁶²⁾ Quark propagators are calculated with the spatial wall source at t_0 with the Dirichlet boundary condition in time at $t = t_0 + 16$. Corresponding hadron masses are given in Table IV.

The coupled channel potential matrix $V_{AB,CD}$ from the NBS wave function for Set 1 is shown in Fig. 19. All diagonal components of the potential matrix have a repulsion at short distance. The strength of the repulsion in each channel, however, varies, reflecting properties of its main component in the irreducible representation of the flavor SU(3). In particular, the $\Sigma\Sigma$ potential has the strongest repulsive core of these three components. It is important to note that off-diagonal parts of the potential matrix satisfy the hermiticity relation $V_{AB,CD} = V_{CD,AB}$ within statistical

	m_π	m_K	m_N	m_Λ	m_Σ	m_Ξ
Set 1	875(1)	916(1)	1806(3)	1835(3)	1841(3)	1867(2)
Set 2	749(1)	828(1)	1616(3)	1671(2)	1685(2)	1734(2)
Set 3	661(1)	768(1)	1482(3)	1557(3)	1576(3)	1640(3)

Table IV. Hadron masses in units of MeV and number of configurations for each set adopted in Sec.7.2.

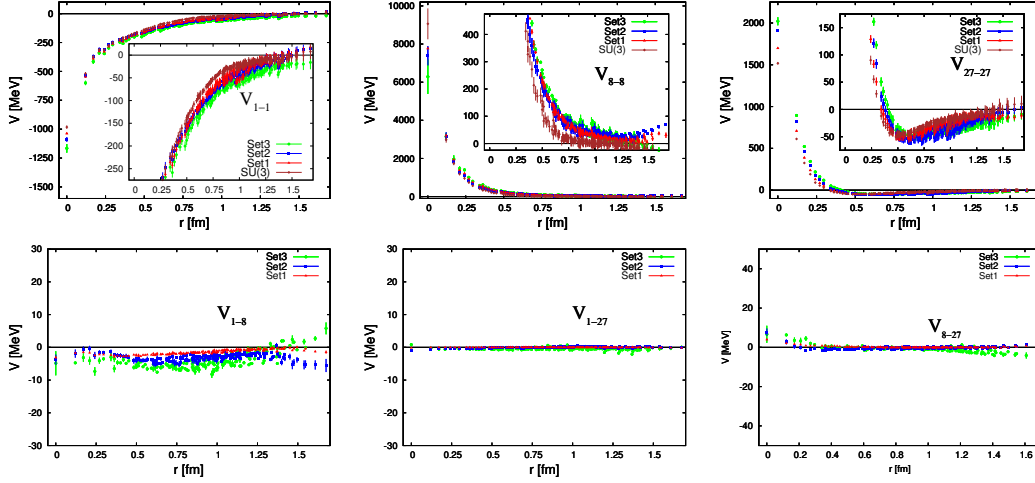


Fig. 20. Transition potentials in the flavor SU(3) IR basis. Red, blue and green symbols correspond to results of Set1, Set2 and Set3, respectively. The result of the flavor SU(3) symmetric limit at the same strange quark mass is also plotted with brown symbols (52).

errors. In addition the off-diagonal parts of $\Lambda\Lambda$ to $N\Xi$ transition $V_{\Lambda\Lambda,N\Xi}$ is much smaller than the other two off-diagonal potentials, $V_{\Lambda\Lambda,\Sigma\Sigma}$ and $V_{N\Xi,\Sigma\Sigma}$.

In order to compare the results of the potential matrix calculated in three configuration sets, the potentials from the particle basis are transformed by the unitary rotation U to those in the flavor SU(3) irreducible representation (IR) basis as

$$V^{IR} = U^\dagger V U = \begin{pmatrix} V_{1,1} & V_{1,8} & V_{1,27} \\ V_{8,1} & V_{8,8} & V_{8,27} \\ V_{27,1} & V_{27,8} & V_{27,27} \end{pmatrix}. \quad (7.12)$$

The potential matrix in the IR basis give a good measure of flavor SU(3) breaking effects since it is diagonal in the SU(3) symmetric limit.

In Fig. 20, the results of the potential matrix in the IR basis are compared among different configuration sets, together with the one in the flavor SU(3) symmetric limit. As the pion mass decreases, the attraction in $V_{1,1}$ potential increases in whole range. While the $V_{8,8}$ potential in the flavor SU(3) limit deviates from others, we do not observe a clear pion mass dependence of the potentials among these flavor breaking cases. In the $V_{27,27}$ potential, we observe the growth of attraction range of potential and the enhancement of repulsive core. The $V_{1,27}$ and $V_{8,27}$ transition potentials are consistent with zero within statistical errors. On the other hand, it is noteworthy that the flavor SU(3) symmetry breaking effect becomes manifest in the $V_{1,8}$ transition potential.

§8. Three-Nucleon Forces

In this section, we expand the scope of our studies from two-nucleon (2N) systems to A -body nucleon systems. Generally speaking, there could exist not only

2-body forces but also 3, 4, \dots A -body forces in such systems. In particular, the determination of three-nucleon forces (3NF) attracts a great deal of interest, since it has been revealed that 3NF play an important and nontrivial role in various phenomena. Some examples include (a) binding energies of light nuclei,⁶³⁾ (b) deuteron-proton elastic scattering experiments,⁶⁴⁾ (c) the anomaly in the oxygen isotopes near the neutron drip-line,⁶⁵⁾ and (d) the nuclear equation of state (EoS) at high density relevant to the physics of neutron stars.⁶⁶⁾ Universal short-range repulsion for three baryons (nucleons and hyperons) has also been suggested in relation to the maximum mass of neutron stars with hyperon core.^{67),68)}

Despite of its phenomenological importance, microscopic understanding of 3NF is still limited. Pioneered by Fujita and Miyazawa,⁶⁹⁾ the long range part of 3NF has been modeled by the two-pion exchange (2π E),⁷⁰⁾ particularly with the Δ -resonance excitation. This 2π E-3NF component is known to have an attractive nature at long distance. An additional repulsive component of 3NF at short distance is often introduced in a purely phenomenological way.⁷¹⁾ An approach based on the chiral effective field theory (EFT) is quite useful to classify the two-, three- and more-nucleon forces and has been studied intensively.⁷²⁾ A completely different approach based on holographic QCD is recently proposed, which obtains repulsive 3NF at short distance.⁷³⁾

To go beyond phenomenology, it is most desirable to determine 3NF directly from the fundamental degrees of freedom (DoF), the quarks and the gluons, on the basis of quantum chromodynamics (QCD). In this section, we present an exploratory study of first-principle lattice QCD calculation of 3NF in the quantum numbers of $(I, J^P) = (1/2, 1/2^+)$ (the triton channel). For details of this study, see Ref. 74).

8.1. Formalism

We consider the NBS wave function $\psi_{3N}(\mathbf{r}, \boldsymbol{\rho})$ extracted from the six-point correlator as

$$\begin{aligned} G_{3N}(\mathbf{r}, \boldsymbol{\rho}, t - t_0) &\equiv \frac{1}{L^3} \sum_{\mathbf{R}} \langle 0 | (N(\mathbf{x}_1)N(\mathbf{x}_2)N(\mathbf{x}_3))(t) \overline{(N'N'N')}(t_0) | 0 \rangle, \quad (8-1) \\ &\xrightarrow{t \gg t_0} A_{3N} \psi_{3N}(\mathbf{r}, \boldsymbol{\rho}) e^{-E_{3N}(t-t_0)}, \quad A_{3N} = \langle E_{3N} | \overline{(N'N'N')}(0) | 0 \rangle, \\ \psi_{3N}(\mathbf{r}, \boldsymbol{\rho}) &\equiv \langle 0 | N(\mathbf{x}_1)N(\mathbf{x}_2)N(\mathbf{x}_3)(0) | E_{3N} \rangle, \quad (8-2) \end{aligned}$$

where E_{3N} and $|E_{3N}\rangle$ denote the energy and the state vector of the 3N ground state, respectively, N (N') the nucleon operator in the sink (source), and $\mathbf{R} \equiv (\mathbf{x}_1 + \mathbf{x}_2 + \mathbf{x}_3)/3$, $\mathbf{r} \equiv \mathbf{x}_1 - \mathbf{x}_2$, $\boldsymbol{\rho} \equiv \mathbf{x}_3 - (\mathbf{x}_1 + \mathbf{x}_2)/2$ the Jacobi coordinates. We consider the following Schrödinger equation of the 3N system with the derivative expansion of the potentials,

$$\left[-\frac{1}{2\mu_r} \nabla_r^2 - \frac{1}{2\mu_\rho} \nabla_\rho^2 + \sum_{i < j} V_{2N}(\mathbf{r}_{ij}) + V_{3NF}(\mathbf{r}, \boldsymbol{\rho}) \right] \psi_{3N}(\mathbf{r}, \boldsymbol{\rho}) = E_{3N} \psi_{3N}(\mathbf{r}, \boldsymbol{\rho}), \quad (8-3)$$

where $V_{2N}(\mathbf{r}_{ij})$ with $\mathbf{r}_{ij} \equiv \mathbf{x}_i - \mathbf{x}_j$ denotes the 2NF between (i, j) -pair, $V_{3NF}(\mathbf{r}, \boldsymbol{\rho})$ the 3NF, $\mu_r = m_N/2$, $\mu_\rho = 2m_N/3$ the reduced masses. 3NF can be determined as

follows. We first calculate $\psi_{3N}(\mathbf{r}, \boldsymbol{\rho})$ and obtain the total potential of the 3N system through Eq. (8.3). Once we obtain all necessary $V_{2N}(\mathbf{r}_{ij})$ by performing (separate) lattice simulations for genuine 2N systems, we can extract $V_{3NF}(\mathbf{r}, \boldsymbol{\rho})$ by subtracting $\sum_{i<j} V_{2N}(\mathbf{r}_{ij})$ from the total potential. The extension to four- and more-nucleon forces can be immediately understood. Note that potentials determined in this way reproduce the energy of the system by construction.

An important remark is that 3NF are always determined in combination with 2NF, and 3NF alone do not make too much sense. Therefore a comparison between lattice 3NF and phenomenological 3NF can be done only at a qualitative level. Rather, our purpose is to determine two-, three-, (more-) nucleon forces systematically, and to provide them as a consistent set.

One of the difficulties in the 3NF study from lattice QCD is that computational costs become exceptionally enormous. Since there are 9 valence quarks, the DoF of color and spinor are significantly enlarged. In addition, the number of diagrams in the Wick contraction tends to diverge with a factor of $N_u! \times N_d!$, where N_u (N_d) are numbers of up (down) quarks in the system. We here develop several techniques to reduce these computational costs. We first take an advantage of symmetries (such as isospin symmetry) to reduce the number of Wick contractions. Second, we utilize a freedom for the choice of a nucleon interpolating operator. In particular, a potential is independent of the choice of a nucleon operator at the source, N' , and we employ the non-relativistic operator as $N' = N_{nr} \equiv \epsilon_{abc}(q_a^T C \gamma_5 P_{nr} q_b) P_{nr} q_c$ with $P_{nr} = (1 + \gamma_4)/2$, which reduces the spinor DoF. Similar techniques are (independently) developed in Ref. 75). On the other hand, a potential depends on the choice of a nucleon operator at the sink, N . As discussed in Sec. 2.4, choosing N corresponds to choosing the “scheme” to calculate nuclear forces. Note that physical observables calculated from these different potentials such as phase shifts and binding energies are unique. In order to determine 3NF and 2NF in the same “scheme”, we employ the same sink operator $N = N_{std} \equiv \epsilon_{abc}(q_a^T C \gamma_5 q_b) q_c$ in the 3NF study, as employed in 2NF. Recall that the choice of $N = N_{std}$ is shown to have good convergence in the derivative expansion in Sec. 4.3, and can be considered to be a good “scheme” for lattice nuclear forces.

We next consider the geometry of the 3N. Since the spacial DoF for general $(\mathbf{r}, \boldsymbol{\rho})$ is too large, it is necessary to find an efficient way to restrict the geometry. In this exploratory study, we propose to use the “linear setup” with $\boldsymbol{\rho} = \mathbf{0}$, with which 3N are aligned linearly with equal spacings of $r_2 \equiv |\mathbf{r}|/2$. In this setup, the third nucleon is attached to (1,2)-nucleon pair with only S-wave. Considering the total 3N quantum numbers of $(I, J^P) = (1/2, 1/2^+)$, the triton channel, the wave function can be completely spanned by only three bases, which can be labeled by the quantum numbers of (1,2)-pair as 1S_0 , 3S_1 , 3D_1 . Therefore, the Schrödinger equation leads to the 3×3 coupled channel equations with the bases of ψ_{1S_0} , ψ_{3S_1} , ψ_{3D_1} . The reduction of the dimension of bases is expected to improve the S/N as well. It is worth mentioning that considering the linear setup is not an approximation: Among various geometric components of the wave function of the ground state, we calculate the (exact) linear setup component as a convenient choice to study 3NF. While we can access only a part of 3NF from it, we plan to extend the calculation to more

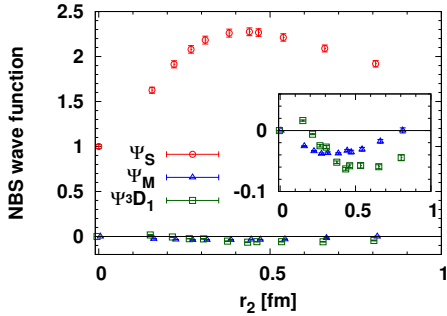


Fig. 21. 3N wave functions at $(t - t_0)/a = 8$. Circle (red), triangle (blue), square (green) points denote ψ_S , ψ_M , ψ_{3D_1} , respectively.

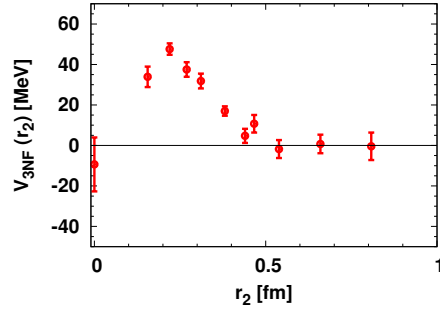


Fig. 22. The effective scalar-isoscalar 3NF in the triton channel with the linear setup obtained at $(t - t_0)/a = 8$. r_2 is the distance between the center and edge in the linear setup.

general geometries step by step, toward the complete determination of the full 3NF.

Finally, we emphasize that 3NF study requires the precise determination of 2NF. This is not surprising because the interactions in 3N systems are mostly dominated by 2NF, and thus small uncertainties in 2NF could easily obscure the signal of 3NF. Note that we generally need precise 2NF in both of parity-even and parity-odd channels, since a 2N-pair inside the 3N system could be either of positive or negative parity. On this point, we have shown that 2NF in parity-even channel can be determined with good precision in lattice QCD. On the other hand, the determination of 2NF in parity-odd channel is much more difficult. While the formulation for parity-odd 2NF is developed in Sec. 4.5, the results are found to suffer from larger statistical errors than parity-even 2NF. This is considered to be a general tendency, since one has to inject a non-zero momentum in the parity-odd 2NF study. Therefore, in the 3NF study, it is essential to suppress the uncertainties originated from parity-odd 2NF.

In order to address this issue, we propose to consider the following channel,⁷⁴⁾

$$\psi_S \equiv \frac{1}{\sqrt{6}} \left[-p_\uparrow n_\uparrow n_\downarrow + p_\uparrow n_\downarrow n_\uparrow - n_\uparrow n_\downarrow p_\uparrow + n_\downarrow n_\uparrow p_\uparrow + n_\uparrow p_\uparrow n_\downarrow - n_\downarrow p_\uparrow n_\uparrow \right], \quad (8.4)$$

which is anti-symmetric in spin/isospin spaces for any 2N-pair. Combined with the Pauli-principle, it is automatically guaranteed that any 2N-pair couples with even parity only. Therefore, parity-odd 2NF vanish in $\langle \psi_S | H | \psi_{3N} \rangle$, where H is the Hamiltonian of the 3N system, and we can extract 3NF unambiguously without referring to parity-odd 2NF. Note that no assumption on the choice of 3D-geometry of \mathbf{r} , $\boldsymbol{\rho}$ is imposed in this argument, and we can take an advantage of this feature for future 3NF calculations with various 3N geometries.

8.2. Numerical results

We employ $N_f = 2$ dynamical configurations with mean field improved clover fermion and RG-improved gauge action generated by CP-PACS Collaboration.³⁹⁾ We

use 598 configurations at $\beta = 1.95$ and the lattice spacing of $a^{-1} = 1.269(14)$ GeV, and the lattice size of $V = L^3 \times T = 16^3 \times 32$ corresponds to $(2.5 \text{ fm})^3$ box in physical spacial size. For u, d quark masses, we take the hopping parameter at the unitary point as $\kappa_{ud} = 0.13750$, which corresponds to $m_\pi = 1.13$ GeV, $m_N = 2.15$ GeV and $m_\Delta = 2.31$ GeV. We use the wall quark source with Coulomb gauge fixing, and periodic (Dirichlet) boundary condition is imposed in spacial (temporal) direction. In order to enhance the statistics, we perform the measurement at 32 source time slices for each configuration, and the forward and backward propagations are averaged. The results from both of total angular momentum $J_z = \pm 1/2$ are averaged as well. Due to the enormous computational cost, we can perform the simulations only at a few sink time slices. Looking for the range of sink time where the ground state saturation is achieved, we carry out preparatory simulations for effective 2NF in the 3N system⁷⁴⁾ in the triton channel at $2 \leq (t - t_0)/a \leq 11$, and find that the results are consistent with each other as long as $(t - t_0)/a \geq 7$.⁷⁴⁾ Being on the safer side, we perform linear setup calculations of 3NF at $(t - t_0)/a = 8$ and 9. We perform the simulation at eleven values of the spacial distance r_2 .

In Fig. 21, we plot the radial part of each wave function of $\psi_S = (-\psi_{1S_0} + \psi_{3S_1})/\sqrt{2}$, $\psi_M \equiv (\psi_{1S_0} + \psi_{3S_1})/\sqrt{2}$ and ψ_{3D_1} obtained at $(t - t_0)/a = 8$. Here, we normalize the wave functions by the central value of $\psi_S(r_2 = 0)$. What is noteworthy is that the wave functions are obtained with good precision, which is quite nontrivial for the 3N system. We observe that ψ_S overwhelms the wave function, and ψ_M , ψ_{3D_1} are much smaller by one to two orders of magnitude. This indicates that higher partial wave components in ψ_S are also strongly suppressed, and the wave function is completely dominated by the component with which all three nucleons are in S-wave in this lattice setup.

We determine 3NF by subtracting 2NF from total potentials in the 3N system. As discussed before, we have only one channel, $\langle \psi_S | H | \psi_{3N} \rangle = \langle \psi_S | H | \psi_S \rangle + \langle \psi_S | H | \psi_M \rangle + \langle \psi_S | H | \psi_{3D_1} \rangle$, which is free from parity-odd 2NF. Correspondingly, we can determine one type of spin/isospin functional form for 3NF. In this study, 3NF are effectively represented in a scalar-isoscalar functional form. This form is an efficient representation, since ψ_S overwhelms the wave function and thus $|\langle \psi_S | V_{3NF} | \psi_S \rangle| \gg |\langle \psi_S | V_{3NF} | \psi_M \rangle|, |\langle \psi_S | V_{3NF} | \psi_{3D_1} \rangle|$ is expected. Note also that the scalar-isoscalar functional form is often employed for the short-range part of 3NF in phenomenological models.⁷¹⁾

In Fig. 22, we plot the results for the effective scalar-isoscalar 3NF at $(t - t_0)/a = 8$. We here include r_2 -independent shift by energy, $\delta_E \simeq 5$ MeV, which is determined by long-range behavior of potentials.⁷⁴⁾ While δ_E suffers from $\lesssim 10$ MeV systematic error, it does not affect the following discussions much, since δ_E merely serves as an overall offset. In order to check the dependence on the sink time slice, we compare 3NF from $(t - t_0)/a = 8$ and 9. While the results with $(t - t_0)/a = 9$ suffer from quite large errors, they are consistent with each other within statistical fluctuations.

Fig. 22 shows that 3NF are small at the long distance region of r_2 . This is in accordance with the suppression of $2\pi E$ -3NF for the heavy pion. At short distance, however, an indication of repulsive 3NF is observed. Note that a repulsive short-

range 3NF is phenomenologically required to explain the properties of high density matter. Since multi-meson exchanges are strongly suppressed for the large quark mass, the origin of this short-range 3NF may be attributed to the quark and gluon dynamics directly. In fact, we recall that the short-range repulsive (or attractive) cores in the generalized two-baryon potentials in the flavor SU(3) limit discussed in Sec.6 are consistent with the Pauli exclusion principle in the quark level.^{45),52)} In this context, it is intuitive to expect that the 3N system is subject to extra Pauli repulsion effect, which could be an origin of the observed short-range repulsive 3NF. Further investigation along this line is certainly an interesting subject in future.

We remark here that the quark mass dependence of 3NF is certainly an important issue, since the lattice simulations are carried out only at single large quark mass. In the case of 2NF, short-range cores have the enhanced strength and broaden range by decreasing the quark mass.¹⁸⁾ We therefore would expect a significant quark mass dependence exist in short-range 3NF as well. In addition, long-range 2π E-3NF will emerge at lighter quark masses, in particular, at the physical point. Quantitative investigation through lattice simulations with lighter quark masses are currently underway.

§9. Meson-baryon interactions

Since our potential method can be naturally extended to meson-baryon systems as well, we consider meson-baryon interactions in this section. The first application is a study on kaon-nucleon (KN) interactions in the $I(J^P) = 0(1/2^-)$ and $1(1/2^-)$ channels. The elastic KN scattering allows us to study the origin of “non-resonant” nuclear forces, since kaon contains $u\bar{s}$ quarks, and these quarks do not annihilate in non-strange nucleons. Therefore, the direct productions of conventional baryon resonances are ruled out. Also, the KN systems in the $I(J^P) = 0(1/2^-)$ and $1(1/2^-)$ channels may be relevant for a possible exotic state Θ^+ ,⁷⁶⁾ whose existence is still controversial.

It is important to emphasize that the one-pion exchange is absent in the KN systems, so that the short- and mid-range interactions dominate the elastic KN scattering. Theoretical studies of the KN interactions so far have been carried out by constituent quark models and meson-exchange models. In both models, it was found that genuine quark-gluon dynamics become important to describe the empirical scattering phase shifts.⁷⁷⁾

To investigate the KN potentials in 2+1 flavor full QCD, we have utilized the gauge configurations of JLDG(Japan Lattice Data Grid)/ILDG(International Lattice Data Grid) generated by PACS-CS Collaboration on a $32^3 \times 64$ lattice.⁷⁸⁾ The renormalization group improved Iwasaki gauge action and non-perturbatively $O(a)$ improved Wilson quark action are used at $\beta = 1.90$, which corresponds to the lattice spacing $a = 0.09$ fm determined from π , K and Ω masses. The physical size of the lattice is about $(2.9 \text{ fm})^3$ and the the hopping parameters are taken to be $\kappa_u = \kappa_d = 0.1370$ and $\kappa_s = 0.1364$. In the present simulation, we adopt the wall source located at t_0 with the Dirichlet boundary condition at time slice $t = t_0 + 32$ in the temporal direction and the periodic boundary condition in each spatial direction.

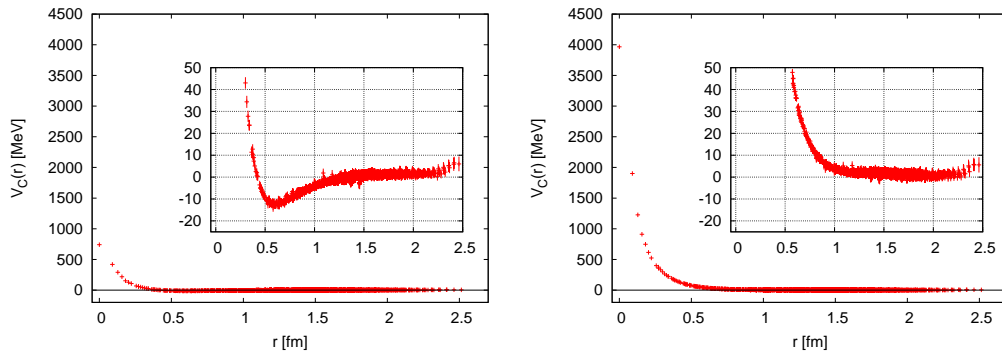


Fig. 23. The LO S-wave central potentials for the KN states in the $I = 0$ (left) and the $I = 1$ channels (right).

The Coulomb gauge fixing is employed at $t = t_0$. The number of gauge configurations used in the simulation is 399. With this setup, we obtain $m_\pi = 705(2)$, $m_K = 793(2)$ and $M_N = 1590(8)$ MeV.⁷⁹⁾

Fig. 23 shows the LO S-wave potential $V(r)$ for the KN state in the $I = 0$ (left) and $I = 1$ (right). The repulsive interactions are observed at short distance in both channels, while the attractive well appears at the mid-distance ($0.4 < r < 0.8$ fm) in the $I = 0$ channel, which is not found in the constituent quark model of hadrons.⁸⁰⁾ These results indicate that there are no bound states in $I(J^\pi) = 0(1/2^-)$ and $1(1/2^-)$ states at $m_\pi \simeq 705$ MeV.

The strong repulsions near origin in the $I = 1$ channel can be expected by the quark Pauli blocking effects. This was first pointed out by Machida and Namiki⁸¹⁾ for the meson-baryon systems. In the $I = 1$ KN (K^+p) state whose configuration is $K^+p \sim (u\bar{s})(uud)$, one of the u -quarks cannot be in the S-state. The strong repulsion at short distance in this channel found in our simulations suggests a manifestation of the quark Pauli blocking. In addition, the repulsive interactions in the S-wave $I = 1$ KN state can be expected much stronger than that of the $I = 0$ KN state in the constituent quark model. Our simulation shows that the repulsion at short distance for the KN potential becomes significantly smaller in the $I = 0$ channel than $I = 1$ channel. This again confirms the expectation from the quark Pauli blocking effects.

Kawanai and Sasaki investigate charmonium-nucleon ($c\bar{c}-N$) interactions using the potential method. Since charmonia do not share the same quark flavor with the nucleon, the $c\bar{c}-N$ interaction is mainly induced by the genuine QCD effect of multi-gluon exchanges and does not manifest the repulsive core near origin. In Ref. 82), the charmonium-nucleon potentials are calculated in quenched QCD on $16^3 \times 48$ and $32^3 \times 48$ lattices at $a \simeq 0.94$ fm at three different values of the light quark mass corresponding to $(m_\pi, m_N) \simeq (640, 1430)$, $(720, 1520)$, $(870, 1700)$ in unit of MeV and one fixed value of the charm quark mass corresponding to $m_{\eta_c} \simeq 2920$ MeV and $m_{J/\psi} \simeq 3000$ MeV. They have found that the effective central $c\bar{c}-N$ potentials clearly exhibit entirely attractive interactions without any repulsion at all distances. Absence of the short range repulsion (the repulsive core) is related to absence of the Pauli exclusion between the heavy quarkonium and the light hadron.

§10. Conclusion

In this report, we reviewed the basic notion of the HAL QCD method for the baryon-baryon (BB) potential and its field-theoretical derivation from the equal-time Nambu-Bethe-Salpeter (NBS) wave function in QCD. The potential $U(\mathbf{x}, \mathbf{y})$ (or the integral kernel of the Schrödinger type equation) in the HAL QCD method has three characteristic features: (i) non-local in relative coordinate, (ii) energy independent, and (iii) scheme dependent. Each of these features has been discussed in detail in this report. By construction, this potential correctly reproduces the scattering phase shift defined from the S-matrix in QCD below the inelastic threshold.

One can construct $U(\mathbf{x}, \mathbf{y})$, once all the NBS wave functions for scattering energies below the inelastic threshold are obtained. In lattice QCD simulations in a finite box, however, it is more practical to adopt the velocity (derivative) expansion of $U(\mathbf{x}, \mathbf{y})$ by its non-locality and determine the local potentials $V(\mathbf{x})$ order by order. This is also in conformity with phenomenological potentials widely used in nuclear physics: An advantage of the HAL QCD method is that one can check the accuracy of this velocity expansion by changing the scattering energies on the lattice. To avoid the well-known problem of exponential error-growth in the temporal correlation of multi hadrons, we have introduced a time-dependent HAL QCD method on the basis of the (imaginary) time Schrödinger type equation. Due to this improved method, we could achieve better construction of the potential as demonstrated in this report.

The leading order (LO) terms of the velocity expansion correspond to the central and tensor potentials: Those for the nucleon-nucleon (NN), hyperon-nucleon (YN) and hyperon-hyperon (YY) interactions have been investigated in full QCD simulations, some of which are recapitulated in this report. The next-to-leading order (NLO) term is the spin-orbit potential: By introducing finite momentum to the nucleons, we could extract the NN spin-orbit force for the first time. The origin of the repulsive core of the NN interaction has been also investigated by extending the SU(2)-flavor to degenerate SU(3)-flavor. The role of the Pauli principle in the quark level to describe the short range part of the interaction becomes clear. In particular, there arises a short range “attractive” core in the flavor singlet channel; we found that it is strong enough to form a bound state, H -dibaryon, in the SU(3) limit.

The HAL QCD method can be extended to the case beyond the inelastic threshold. This is necessary to treat the YN and YY interactions with SU(3)-flavor symmetry breaking. We have presented its application to $(S, I) = (-2, 0)$ system and derived the coupled channel potentials among $\Lambda\Lambda$, $N\Xi$ and $\Sigma\Sigma$. The HAL QCD method is also applied to the three-nucleon force relevant for the extra binding of finite nuclei and also for the maximum mass of neutron star, and to the meson-baryon interactions relevant for the meson-baryon resonances and the pentaquark.

So far, our full QCD simulations of the BB interactions are performed at non-zero lattice spacing on a finite volume with relatively large quark masses. We therefore need careful studies of systematic errors on finite volume effect, quark mass dependence and the lattice spacing effect. Among others, the most important direction is to carry out (2+1)-flavor simulations on a large volume (e.g. $L = 6 - 9$ fm) at physical quark mass ($m_\pi = 135$ MeV) to extract the realistic BB and BBB

potentials. Such simulations are planned at 10 PFlops “K computer” in Advanced Institute for Computational Science (AICS), RIKEN.

If it turns out that the program described in this paper indeed works in lattice QCD at the physical quark mass, it would be a major step toward the understanding of atomic nuclei and neutron stars from the fundamental law of the strong interaction, the quantum chromodynamics.

Acknowledgement

We thank CP-PACS, JLQCD and PACS-CS Collaborations and ILDG/JLDG for providing us the gauge configurations.^{34),39),53),83),84)} We are grateful for the authors and maintainers of CPS++,⁸⁵⁾ a modified version of which is used for measurement done in this work. The numerical simulations have been carried out on Blue Gene/L at KEK, T2K at University of Tsukuba and at University of Tokyo, SR16000 at YITP in Kyoto University, and SX9 and SX8R at RCNP in Osaka University. This research is supported in part by Grant-in-Aid for Scientific Research on Innovative Areas(No.2004:20105001,20105003) and for Scientific Research(C) 23540321, 24740146, JSPS 21-5985 and SPIRE (Strategic Program for Innovative REsearch).

References

- 1) M. Taketani et al., *Prog. Theor. Phys. Suppl.* 39 (1967) 1
- 2) N. Hoshizaki et al., *Prog. Theor. Phys. Suppl.* 42 (1968) 1
- 3) G. E. Brown and A. D. Jackson, *Nucleon-nucleon Interaction*, (North-Holland, Amsterdam, 1976).
- 4) R. Machleidt, *Adv. Nucl. Phys.* 19 (1989) 189
- 5) R. Machleidt and I. Slaus, *J. Phys.* G27 (2001) R69
- 6) R. Machleidt, *Phys. Rev. C* 63 (2001) 024001
- 7) V. G. J. Stoks, R. A. M. Klomp, C. P. F. Terheggen and J. J. de Swart, *Phys. Rev. C* 49 (1994) 2950
- 8) R. B. Wiringa, V. G. J. Stoks and R. Schiavilla, *Phys. Rev. C* 51 (1995) 38
- 9) N. Ishii, S. Aoki and T. Hatsuda, *Phys. Rev. Lett.* 99 (2007) 022001 [arXiv:nucl-th/0611096].
- 10) H. Yukawa, *Proc. Math. Phys. Soc. Japan* 17 (1935) 48
- 11) M. Taketani, S. Machida and S. Onuma, *Prog. Theor. Phys.* 7 (1952) 45
- 12) R. Jastrow, *Phys. Rev.* 81 (1951) 165
- 13) R. Tamagaki et al., *Prog. Theor. Phys. Suppl.* 112 (1993) 1
- 14) H. Heiselberg and V. Pandharipande, *Ann. Rev. Nucl. Part. Sci.* 50 (2000) 481
- 15) J. M. Lattimer and M. Prakash, *Phys. Rep.* 333 (2000) 121
- 16) M. Lüscher, *Nucl. Phys. B* 354 (1991) 531
- 17) S. Aoki, T. Hatsuda and N. Ishii, *Comput. Sci. Dis.* 1 (2008) 015009 [arXiv:0805.2462 [hep-ph]].
- 18) S. Aoki, T. Hatsuda and N. Ishii, *Prog. Theor. Phys.* 123 (2010) 89 [arXiv:0909.5585 [hep-lat]].
- 19) A. Gal, O. Hashimoto and J. Pochodzalla, *Special Issue on Progress in Strangeness Nuclear Physics*, *Nucl. Phys. A* **881** (2012).
- 20) S. R. Beane, W. Detmold, K. Orginos and M. J. Savage, *Prog. Part. Nucl. Phys.* **66**, 1 (2011) [arXiv:1004.2935 [hep-lat]].
- 21) N. Ishizuka, *PoS LAT2009* (2009) 119
- 22) W. Królkowski and J. Rzewuski, *Nuovo Cimento* 4 (1956) 1212
- 23) R. Tamagaki and W. Watari, *Prog. Theor. Phys. Suppl.* 39 (1967) 23
- 24) S. Okubo and R. E. Marshak, *Ann. Phys.* 4 (1958) 166
- 25) K. Nishijima, *Phys. Rev.* 111 (1958) 153
- 26) W. Zimmermann, *Nuovo Cim.* 10 (1958) 597 ; MPI-PAE/PTh-61/87 (1987), unpublished.
- 27) R. Haag, *Phys. Rev.* 112 (1958) 669
- 28) S. Aoki, J. Balog and P. Weisz, *JHEP* 1005 (2010) 008 [arXiv:1002.0977 [hep-lat]].
- 29) S. Aoki, J. Balog and P. Weisz, *JHEP* 1009 (2010) 083 [arXiv:1007.4117 [hep-lat]].
- 30) S. Aoki, J. Balog, T. Hatsuda, N. Ishii, K. Murano, H. Nemura and P. Weisz, *PoS LAT2008* (2008) 162 [arXiv:0812.0673 [hep-lat]].

- 31) K. Murano, N. Ishii, S. Aoki and T. Hatsuda, *PoS LAT2009* (2009) 126 [arXiv:1003.0530 [hep-lat]].
- 32) K. Murano, N. Ishii, S. Aoki and T. Hatsuda, *PoS LAT2010* (2010) 150 [arXiv:1012.3814 [hep-lat]].
- 33) K. Murano, N. Ishii, S. Aoki and T. Hatsuda, *Prog. Theor. Phys.* **125**, 1225 (2011) [arXiv:1103.0619 [hep-lat]].
- 34) S. Aoki et al. [PACS-CS Collaboration], *Phys. Rev. D* **79** (2009) 034503 [arXiv:0807.1661 [hep-lat]].
- 35) S. Aoki et al. [PACS-CS Collaboration], *Phys. Rev. D* **81** (2010) 074503 [arXiv:0911.2561 [hep-lat]].
- 36) N. Ishii, S. Aoki and T. Hatsuda, *PoS LATTICE2008* (2008) 155 [arXiv:0903.5497 [hep-lat]].
- 37) N. Ishii et al. [HAL QCD Collaboration], *Phys. Lett. B* **712**, 437 (2012) [arXiv:1203.3642 [hep-lat]].
- 38) <http://www.nm-online.org/>
- 39) A. Ali Khan et al. [CP-PACS Collaboration], *Phys. Rev. D* **65**, 054505 (2002) [Erratum-ibid. *D* **67**, 059901 (2003)] [arXiv:hep-lat/0105015].
- 40) CP-PACS Collaboration, <http://www.jldg.org/ildg-data/CPACSCONFIG.html>
- 41) B. F. Gibson and E. V. Hungerford, *Phys. Rept.* **257**, 349 (1995).
- 42) Reviewed in O. Hashimoto and H. Tamura, *Prog. Part. Nucl. Phys.* **57** (2006) 564
- 43) H. Nemura, for HAL QCD Collaboration, arXiv:1203.3320 [hep-lat].
- 44) N. Ishii [PACS-CS Collaboration and HAL-QCD Collaboration], *PoS LAT2009*, 019 (2009) [arXiv:1004.0405 [hep-lat]].
- 45) Reviewed in M. Oka, K. Shimizu and K. Yazaki, *Prog. Theor. Phys. Suppl.* **137** (2000) 1 ; Y. Fujiwara, Y. Suzuki and C. Nakamoto, *Prog. Part. Nucl. Phys.* **58** (2007) 439
- 46) J.K. Ahn, et al., *Phys. Lett. B* **633** (2006) 214
- 47) K. Nakazawa, *Nucl. Phys. A* **639** (1998) C345
- 48) T. Fukuda, et al., *Phys. Rev. C* **58** (1998) 1306
- 49) P. Khaustov, et al., *Phys. Rev. C* **61** (2000) 054603
- 50) See for example, http://j-parc.jp/NuclPart/index_e.html
- 51) H. Nemura, N. Ishii, S. Aoki and T. Hatsuda, *Phys. Lett. B* **673** (2009) 136 [arXiv:0806.1094 [nucl-th]].
- 52) T. Inoue et al. [HAL QCD collaboration], *Prog. Theor. Phys.* **124** (2010) 591 [arXiv:1007.3559 [hep-lat]].
- 53) CP-PACS and JLQCD Collaborations, <http://www.jldg.org/ildg-data/CPACSCONFIG+JLQCD.html>
- 54) T. Inoue et al. [HAL QCD Collaboration], *Phys. Rev. Lett.* **106** (2011) 162002 [arXiv:1012.5928 [hep-lat]].
- 55) T. Inoue [for HAL QCD Collaboration], arXiv:1111.5098 [hep-lat].
- 56) T. Inoue et al. [HAL QCD Collaboration], *Nucl. Phys. A* **881** (2012) 28 [arXiv:1112.5926 [hep-lat]].
- 57) Reviewed in J. Schaffner-Bielich, *Nucl. Phys. A* **835** (2010) 279 [arXiv:1002.1658 [nucl-th]].
- 58) S. R. Beane et al. [NPLQCD Coll.], *Phys. Rev. Lett.* **106** (2011) 162001 [arXiv:1012.3812 [hep-lat]].
- 59) S. R. Beane et al. [NPLQCD Collaboration and NPLQCD Collaboration and NPLQCD Collaboration], “The Deuteron and Exotic Two-Body Bound States from Lattice QCD,” arXiv:1109.2889 [hep-lat].
- 60) N. Ishii, for HAL QCD Collaboration, *PoS LATTICE2010* (2010) 145 [arXiv:1102.5408 [hep-lat]].
- 61) S. Aoki et al. [HAL QCD Collaboration], *Proc. Japan Acad. B* **87** (2011) 509 [arXiv:1106.2281 [hep-lat]].
- 62) K. Sasaki or HAL QCD Collaboration, *PoS LATTICE2010* (2010) 157 [arXiv:1012.5684 [nucl-th]].
- 63) S. C. Pieper, *Riv. Nuovo Cim.* **31**, 709 (2008) [arXiv:0711.1500 [nucl-th]].
- 64) K. Sekiguchi et al., *Phys. Rev. C* **83**, 061001 (2011) [arXiv:1106.0180 [nucl-ex]].
- 65) T. Otsuka, T. Suzuki, J. D. Holt, A. Schwenk and Y. Akaishi, *Phys. Rev. Lett.* **105**, 032501 (2010) [arXiv:0908.2607 [nucl-th]].
- 66) A. Akmal, V. R. Pandharipande and D. G. Ravenhall, *Phys. Rev.* **C58**, 1804 (1998) [nucl-th/9804027].
- 67) S. Nishizaki, T. Takatsuka and Y. Yamamoto, *Prog. Theor. Phys.* **108**, 703 (2002).
- 68) T. Takatsuka, S. Nishizaki and R. Tamagaki, *Prog. Theor. Phys. Suppl.* **174**, 80 (2008).
- 69) J. Fujita and H. Miyazawa, *Prog. Theor. Phys.* **17** (1957) 360
- 70) S. A. Coon and H. K. Han, *Few Body Syst.* **30**, 131 (2001) [arXiv:nucl-th/0101003].
- 71) S. C. Pieper, V. R. Pandharipande, R. B. Wiringa and J. Carlson, *Phys. Rev. C* **64**, 014001 (2001) [arXiv:nucl-th/0102004].
- 72) S. Weinberg, *Phys. Lett. B* **295**, 114 (1992) [arXiv:hep-ph/9209257]. See also a review,

- E. Epelbaum, H. -W. Hammer, U. -G. Meissner, *Rev. Mod. Phys.* **81**, 1773-1825 (2009) [arXiv:0811.1338 [nucl-th]].
- 73) K. Hashimoto and N. Iizuka, *JHEP* **1011**, 058 (2010) [arXiv:1005.4412 [hep-th]].
- 74) T. Doi *et al.* (HAL QCD Coll.), *Prog. Theor. Phys.* **127** (2012) 723 [arXiv:1106.2276 [hep-lat]].
- 75) T. Yamazaki, Y. Kuramashi and A. Ukawa, [PACS-CS Collab.], *Phys. Rev.* **D81**, 111504 (2010) [arXiv:0912.1383 [hep-lat]].
- 76) T. Nakano *et al.* [LEPS Collaboration], *Phys. Rev. Lett.* **91**, 012002 (2003) [arXiv:hep-ex/0301020].
- 77) K. Hashimoto, *Phys. Rev. C* **29**, 1377 (1984).
- 78) PACS-CS Collaboration, <http://www.jldg.org/ildg-data/PACSCSconfig.html>
- 79) Y. Ikeda *et al.* [HAL QCD Collaboration], arXiv:1111.2663 [hep-lat].
- 80) T. Barnes and E. S. Swanson, *Phys. Rev. C* **49**, 1166 (1994).
- 81) S. Machida and M. Namiki, *Prog. Theor. Phys.* **33**, 125 (1965).
- 82) T. Kawanai and S. Sasaki, *Phys. Rev. D* **82**, 091501 (2010) [arXiv:1009.3332 [hep-lat]].
- 83) M. G. Beckett, B. Joo, C. M. Maynard, D. Pleiter, O. Tatebe and T. Yoshie, *Comput. Phys. Commun.* **182** (2011) 1208 [arXiv:0910.1692 [hep-lat]].
- 84) <http://www.lqcd.org/ildg>, <http://www.jldg.org>
- 85) CPS++. <http://qcdoc.phys.columbia.edu/cps.html> (maintainer: Chulwoo Jung)